

Department of Mechanical Engineering

Final Year Project: Final Report

Machine Learning for Defect Detection in 3D Printing Process

Author:

Boon Ho

(01235856)

Supervisor:

Dr. Paul Hooper

Date:

4th June 2020

Word Count:

11521/12000

Acknowledgements

I would like to express my gratitude to my final year project supervisor, Dr. Paul Hooper for his guidance and advice. Those scheduled weekly meetings and brainstorming sessions we had were immensely helpful. Not forgetting the PhDs, Harry and Seb, for which their suggestions have often been my source of inspiration.

Abstract

The formation of defects in laser powder bed fusion product is closely related melt pool dynamics. The occurrence of melt pool anomalies such as plume ejection or spattering could result in defects formation. In this project, two machine learning frameworks are proposed for melt pool anomalies detection and classification.

One class learning with deep convolutional autoencoder was proposed as the first framework for anomalies detection. In this framework, the autoencoder was trained to specialise in reconstructing normal melt pool images. Failing to reconstruct anomalous melt pool images, the autoencoder commits a high reconstruction error. Following that, an appropriate RE threshold was determined through the use of a receiver operating characteristic (ROC) graph. The performance of the autoencoder was also compared with the data pre-sieving model and a newly instantiated autoencoder trained on further cleaned training dataset. This framework does show some promising melt pool anomaly detection performance.

The second framework proposed was an automated features extraction framework. Instead of manual features extraction, this framework utilises the data compressing capability of a disentangled variational autoencoder to extract latent components related to the tail length, size and roundness of melt pool. K-Means Clustering algorithm was then used to compute the distance of data points from their respective cluster's centroid in the latent space. This distance -based metric was used as an anomaly metric. Furthermore, three supervised classifiers were trained based on these melt pool encodings. Subsequently, this framework enabled the detection of plume, large melt pools and melt pools with unstable tail.

With the classified melt pool anomalies, a case study was conducted to investigate on the formation of build defects. Based on the spike in anomaly metrics, various melt pool anomalies have been detected. It was hypothesised that the build defects were, to a certain extent, caused by these anomalies. Furthermore, the correlation analysis shows slight positive association between the size of melt pools and the average surface depth.

Finally, future work will focus on training and validating the models with a more diverse melt pool images dataset. With known limitation, the resulting models will then be generic enough to cope for melt pool images produced under different printing parameters.

Contents

1	Project Background and Literature Review	1
1.1	Additive Manufacturing.....	1
1.2	Objectives	2
1.3	Melt Pool Dynamics and Defects Formation.....	2
1.4	Machine Learning for Anomalies Detection.....	4
1.5	Similar Work	5
2	Introduction to data	7
3	Exploratory Data Analysis.....	8
3.1	Random Visualisations.....	8
3.2	Metrics for Visualisations	9
3.3	Region Properties Features Extraction	12
4	One Class Learning Framework	14
4.1	Data Filtering	14
4.2	Autoencoder.....	17
4.3	Anomalies Detection	20
4.4	Anomalies Detection Performance Evaluation	23
4.5	Discussion of Framework.....	27
5	Automated Features Extraction Framework	29
5.1	Data Pre-processing.....	29
5.2	Disentangled Variational Autoencoder (β -VAE).....	30
5.3	Features Extraction.....	31
5.4	Anomalies Detection	33
5.5	Anomalies Classification Performance Evaluation	35
5.6	Discussion of Framework.....	36
6	Results and Discussions	38
6.1	Methods	38
6.2	Results	42
6.3	Discussions: Overlaid results	49
7	Conclusion and Future Work Suggestion	50
7.1	Conclusion	50
7.2	Future work suggestions	51
8	References	52

1 Project Background and Literature Review

1.1 Additive Manufacturing

Additive manufacturing (AM, also known as 3D printing) refers to a variety of manufacturing techniques which produce a 3D component in a layer-by-layer additive manner. AM offers a wide range of advantages relative to conventional manufacturing methods. Firstly, material wastage which is a common issue in conventional manufacturing techniques can be avoided in AM due its layer-wise printing methodology. More importantly, AM offers unprecedented design freedom as manufacturing parts with complex geometries can be printed out easily. This also means that parts design and manufacturing process can be optimised for higher structural strength-to-weight ratio. In terms of application, the advantages of AM made it very attractive to industries such as medical engineering, automotive and aerospace.

In this project, the AM technique of interest is known as laser powder bed fusion, LPBF. In LPBF, a focused laser beam scans through a predefined path and prints out the cross section of the final part layer by layer. Firstly, the metallic powder will be spread uniformly by a roller on top of the printing platform. During the scanning process, the high energy density from the laser beam creates a localised region where the metallic powder actively melts and fuses together, known as melt pool. Once the layer is done printing, the roller will spread a new layer of powder on top of the solidified cross section. Both the new layer and solidified layer will be fused together in subsequent scanning, and the whole process continues until the end of printing.

Whilst AM offers great benefits, the inconsistent quality of parts produced due to defects formation greatly hinders the wide adoption for mass manufacturing. Similar to other types of AM techniques, LPBF products also suffer from defects formation. The formation of these defects is primarily governed by the local microstructure development on the build which, in turn, is very sensitive to the local temperature field. In short, unfavourable printing conditions could promote the formation of defects.

Despite LPBF being a relatively mature technology, optimising the printing process parameters and parts design are mostly conducted iteratively and empirically [1]. This is because the localised and rapidly changing temperature field poses a challenge for deeper understanding of the defect formation process. To resolve the temperature profile of the melt pool temporally and spatially, a commercial Renishaw AM250 LPBF is modified [1]. Two high speed cameras are incorporated and the ratio of light intensities captured is then used to resolve the melt pool temperature's profile.

With this modification, the high-speed thermal imaging system allows coaxial tracking of the melt pool along its scan path. Videos of the printing process are then recorded for further analysis.

1.2 Objectives

With the melt pool frames collected, the project focuses extensively on analysing the melt pool dynamics through the lens of machine learning models. Specifically, the main aim of the project is to design a set of metrics or data processing frameworks to robustly describe the state of a melt pool. Successful detection and classification of anomalous LPBF melt pool are of paramount importance and can be seen as the prerequisites for subsequent defects investigation.

The objectives of the project are listed as follow:

1. Explore different machine learning models capable of detecting and classifying anomalous melt pools under different scans.
2. Evaluate the machine learning models performance with multiple test data.

As the long-term vision of this work is to incorporate successfully trained models into the in-situ monitoring system, considerations such as data processing speeds will also be taken into account when designing various frameworks.

1.3 Melt Pool Dynamics and Defects Formation

The formation of defects in LPBF products is governed by the microstructure evolution caused by the dynamics of melting pool during the printing process. As a consequence of heat, momentum and mass transfers, the temperature profile in the vicinity of the melt pool varies spatially and temporally. The melt pool dynamics is in turn sensitive to factors such as choice of materials, printing process parameters and powder morphology. Optimising these parameters is often carried out with experimental trials which can be inefficient and time consuming. Even with the correct set of parameters, defects could still form unexpectedly [2]. Hence, the study of the relationship between melt pool dynamics and defects formation is of paramount importance to help establish a theoretical guideline for parameters optimisation and defect detection.

In the past, various computational modelling, simulations and experiments have been conducted to model the dynamics of melt pool. Khairallah et al. [3] modelled the melt pool dynamics with a three-dimensional powder-scale model with randomly distributed powder particles. This study has provided profound understandings on melt pool dynamics and several defect formation mechanisms. In particularly, the dominant effects of surface tension (Marangoni effect) and of vapour recoil pressure in different melt flow regions have been formulated. The model has also

enabled explanations for the formation of denudation, spatter and pore defects. Based on this work, the melting pool is divided into three regions, the topological depression, transitional and tail-end regions, as illustrated in Figure 1.3.1:

1. The **topological depression**. This region is located directly under the laser beam and it has the highest temperature in the melt pool. Recoil pressure arising from melt vapour dominates over surface tension in this region. Consequently, the recoil pressure causes liquid to escape away from the depression zone. This promotes spattering and an effect which is similar to keyholing observed in laser welding [4]. Away from the depression zone in the rearward direction, the drop in temperature causes surface tension to dominate over recoil pressure. This reverses the flow direction and melt liquid flows back to fill up the topological depression. As a result of the abrupt change in flow direction, the rear of the depression zone collapses, potentially trapping gas bubbles within. These bubbles could coalesce and form even bigger pores when the melt liquid solidifies.
2. The **transitional zone**. In this region, the melt liquid overflows out of the melt track. The overflowed liquid then came into contact with nearby partially melted particles. The surface tension then entrains the neighbouring particles into the transitional zone. This forms regions with side tracks or bridges laterally connected to the melt flow known as denuded zone as shown in Figure 1.3.1. Denudation could promote defects in the form of pores when the next layer is deposited or when the entrained particles are partially melted and have voids in between them. Denudation is also observed experimentally in [5] where entrained particles are ejected out as spatter particles or droplets and redistributed to elsewhere in the powder bed. These material spatter, especially the larger droplets are unfavourable for mechanical properties of the final build [6,7]. Aside from particles entrainment, [8] also found that powder particles in the denuded zone can be blown away from the melt pool, thus reducing the amount of material available for fusion.
3. The **tail-end region**. The melt pool breaks up into the smaller droplet form segments. The region exhibits fluctuations due to balling effect. The instability, however, can be controlled by adjusting the laser speed for a given power.

Plume ejection is another possible form of melt pool instability. Bidare et al. [8] observed that the inclination of plume under different power and scan speeds affects the flow in the proximity of the melt pool. This may result in more severe fused powder agglomeration and locally altered powder particles distribution. Consequently, different mass, heat and momentum transfer will be involved.

Furthermore, undesired melt pool dimensions can give rise to phenomena [9] such as over- and under-melting. Whilst [10] under-melting may result in porosity in the build which has a negative impact on tensile and fatigue strength, over-melting can lead to compromised dimensional accuracy and surface finishing. Melt pool dimensions can also influence the solidification process and hence the microstructural characteristics of the build. Gockel et al. [11] emphasized on having controlled melt pool dimensions for predictable microstructure and mechanical properties such as fatigue behaviour.

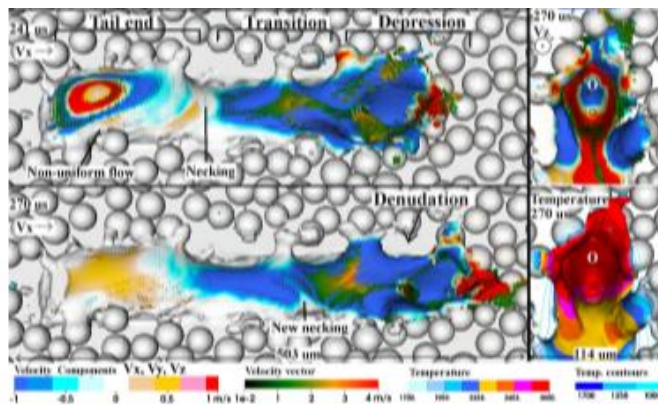


Figure 1.3.1 [3] 3D powder-scale model showing the depression, transition, tail-end regions and the phenomena of denudation.

1.4 Machine Learning for Anomalies Detection

Machine learning [12] is a data driven modelling approach and can be used as an alternative to conventional domain knowledge-driven data analysis. In conventional modelling, the problem of interest is studied in detail for the formulation of a mathematical model which is able to capture the underlying physics and represent the reality accurately. In contrast, a machine learning approach replaces the step of acquiring understanding of the problem with a potentially easier data collection task. With sufficient representative examples, a trained machine learning model will be able to generalise well for unseen data. In the machine learning paradigm, most models can be categorised into supervised and unsupervised learning types. In the supervised approach, the training data points are associated with desired outputs, either in the form of continuous figures for regression or labels for classification problems. Examples of supervised models are support vector machine, decision tree and k-nearest neighbours. On the other hand, unsupervised models operate on unlabelled data points and generally helps to discover the underlying data pattern. Most unsupervised models operate based on clustering methods, for instance, k means clustering and gaussian mixture models, although recently the usage of generative models such as autoencoder has also been explored in the field of [13] manufacturing defect detection.

In broad sense, anomalies [14] are data points with patterns that deviate from those of normal instances. Anomalies detection is critical as these unusual data points could signify the occurrence of various unfamiliar events. In the context of melt pool dynamics, anomalies such as spatter particles and plume ejection could directly or indirectly promote the formation of various defects. Hence, by designing a proper anomaly metric, one would be able to quantify the degree of anomaly for melt pools. Subsequently, classification can then be carried out on the detected anomalies. The metric would also enable a within-class-comparison for the classified melt pool anomalies.

Most anomaly detection models such as classification-based [15] and clustering-based models [16], operate based on constructed profiles for normal instances. Data points which do not conform to these profiles will then be flagged as anomalies. One class learning framework is an example which falls under this category. Under this framework, there is an assumption that normal instances are typically similar to each other and models will be trained to specialise in recognizing those instances. One-class support vector machine [17] and autoencoders are examples of one class learning models. As an example of one class learning usage in manufacturing defect detection, a one class learning autoencoder was employed for soldering defect detection in [13].

Aside from normal instances profiling, there are models which explicitly isolate anomalous instances without relying on any profiling. The idea of detecting outliers with a data-induced tree, termed as isolation tree, was introduced in [14]. Based on this idea, anomalous data points are defined as the minorities which are different from the normal instances. As such, they are more susceptible to isolation and will generally be isolated nearer to the root of the tree. Density based approaches [18] such as density-based clustering method (DBSCAN) and local outlier factor (LOF) can be used to how detect data points which are locally different to their surrounding neighbourhood. Most of these anomaly detectors are unsupervised models and hence they do not require any explicit data labelling.

1.5 Similar Work

As discussed, anomalies present in powder bed fusion process such as plume and spatter particles could be detrimental to the mechanical properties of the final product. Prior to investigating the real effects of different melt pool dynamics, it is necessary to develop a process monitoring system which is able to detect any arising anomaly.

The most commonly reported monitoring frameworks are ‘co-axial’ and ‘off-axial’. In the co-axial setup, the melt pool optical signal is tracked continuously, hence having the melt pool maintained

at the centre of the image throughout the printing process [1]. For example, the co-axial configuration is suitable for resolving the local temperature field [1] and the [19] morphological changes of melt pool. On the other hand, the off-axial configurations provide a more comprehensive information which usually encompasses the interactions of melt pool with its surroundings such as [20] the temperature distribution of the melt pool track. The monitoring methods are not just limited to optical signals. In fact, acoustic [21] and ultrasonic [22] sensors have also been used as part of the powder bed fusion monitoring system. With the captured signals, various statistical analyses can be performed for anomalies detection and classification.

Repossini et al. [23] investigated the viability of including spatter-related information for the classification of different energy density conditions such as over-melting and under-melting. A logistic regression model was used for the classification purposes. With the inclusion of various statistical descriptors describing the spattering behaviour, a significant increase in the model's capability was realised.

Zhang [24] et. al conducted a preliminary study on the suitability of handcrafted features related to plume, melt pool and spatter from streams of high-speed camera images for melt track quality classification by support vector machine (SVM). Notably, the test results suggested that the SVM model is suitable to be used for quality level identification and further dimensionalities reduction with principal component analysis (PCA) shows potential improvement of SVM's performance. However, the convolutional neural network (CNN) showed even better performance in most of the prediction results when trained on raw images. The study has also highlighted the potential computational savings with the deployment of CNN for industrial on-line monitoring use since CNN learns the underlying features directly and automatically from the raw images.

Previous discussions span a variety of supervised frameworks in LPBF monitoring. In [25], an unsupervised approach consisting of iterative statistical descriptor update during printing process was proposed. The proposed approach monitors the printing process and localises defective areas within a layer through a layer wise image data analysis. A statistical descriptor based on PCA is applied to the image data to identify anomalous molten area. The defect detection process can then be extended with the usage of k-means clustering on the descriptor's spatial distribution. It is worth noting that the proposed defect detection approach was based on the build pixel intensities from the build rather than the melt pool dynamics.

2 Introduction to data

Initially, two types of datasets supplied are used for analyses. Below are some descriptions and the use cases of these datasets.

1. The **melt pool images** dataset comprises of video frames of the printing process. These video frames are either in their raw form or in the form of resolved temperature profiles. The exploratory data analysis, anomalies detection and classification work were all carried out on the temperature images due to their higher resolutions.
2. The instantaneous locations of the laser spots were also provided in the form of cartesian coordinates in the **positional dataset**. This dataset provides location reference to help determine whether a given video frame corresponds to temperature profile resolved during straight scan, inner border scan, outer border scan or turning. Note that certain positional datasets can be noisy.
3. Additional datasets such as microscopic image of the topmost build layer and depth data. These data were used to relate the occurrence of melt pool anomalies and formation of defects.

Several build data were collected at different times while the project was ongoing, some of which were used for data processing frameworks formulation and the remaining ones for testing out the whole framework. Following are some details of these data:

1. Build 2 and Build 3 (older datasets): Both datasets were generated under different printing focus heights at early stage of the project. These datasets consist of melt pool images and positional dataset. They are mostly used for anomalies detection and classification frameworks formulation. Some machine learning models performance were quantified based on these datasets.
2. Build 2 and Build 3 (new datasets). These new multilayer datasets were collected later on, with build 2 generated from the printing of nine rectangular blocks and build 3 collected from the printing of a cylindrical pin. The focus heights of build 2 is restricted to just -4mm, +4mm and 8mm. One of the topmost layer microscopic images of build 2 was used for defects and anomaly analysis.

3 Exploratory Data Analysis

In the exploratory data analysis (EDA), some melt pools were inspected to gain an early understanding of the dataset. This is crucial to build up some expectations with the types of potential anomalies in the dataset. Note EDA was carried out on the older datasets.

3.1 Random Visualisations

Video frames of melt pools are randomly sampled for visualisations as shown in Figure 3.1.1. A few anomalies such as plume and spatter particles have been spotted around the melt pool. Typically, the resolved temperature field of melt pool with plume ejection (Figure 3.1.1(b)) is manifested as a large blob with irregular shape whereas spatter particles (Figure 3.1.1(c)) are usually smaller than the melt pool. Phenomena of melt pools having unstable or separating tail have also been observed as depicted in Figure 3.1.2(a). The consequences of having plume, unstable tail and spatter particles on the build quality have been discussed in Section 1.3.

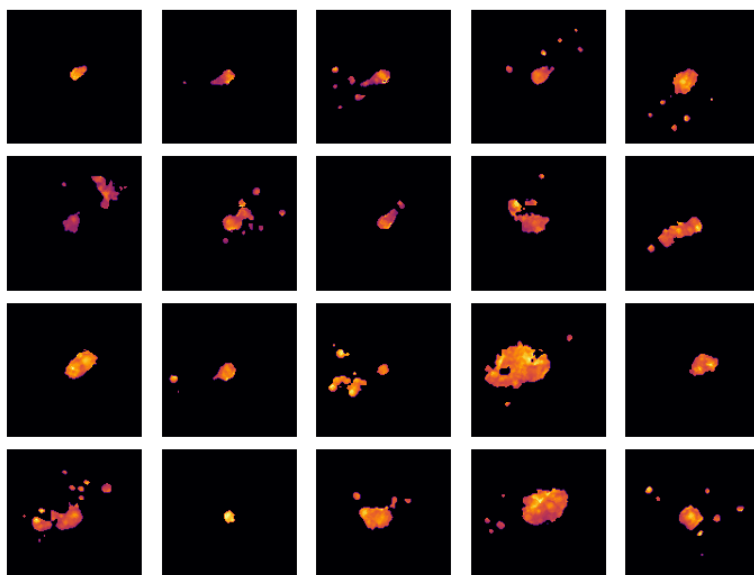


Figure 3.1.1 Melt pool video frames randomly sampled for visualisations

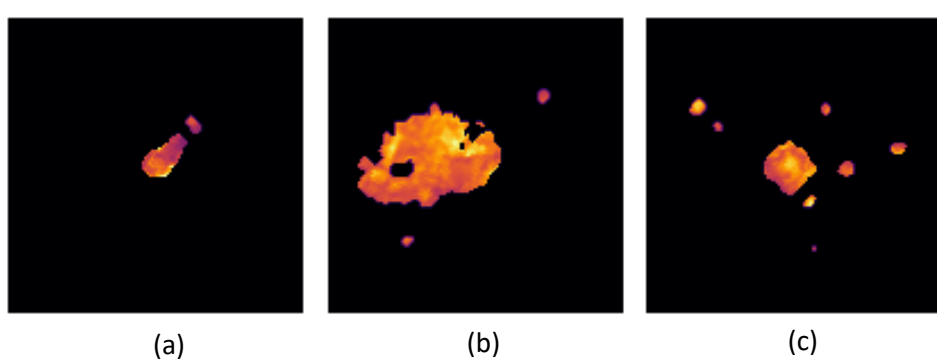


Figure 3.1.2 (a) Melt pool tail separation, (b) plume and (c) spatter particles around a melt pool.

3.2 Metrics for Visualisations

Given the size of the dataset, it is impractical to inspect every video frame manually. A standardized and quick data exploration technique was hence deemed necessary. Three different metrics were developed based on the early understandings on the dataset. Each metric aims to provide different insights on the video frames via data visualizations. These metrics are the subregion mean (SRM), the pixel intensity standard deviation (SD) and the proportion of bright pixels (PBP) for a given video frame.

The **SRM** metric measures the scatteredness of the spatter particles present in a given frame. To compute this metric, a given image is partitioned into top, bottom, left and right subregions as shown in Figure 3.2.1. Then, the mean pixel intensities from all four subregions are summed up. Subregions which contain many bright pixels will contribute additively to the final sum with their high mean pixel intensity. Conceptually, this means that the frames with very scattered spatter particles will have higher chance of having spatter particles ended up in the subregions, hence giving rise to high SRM, while clean and focused melt pools should give a low SRM.

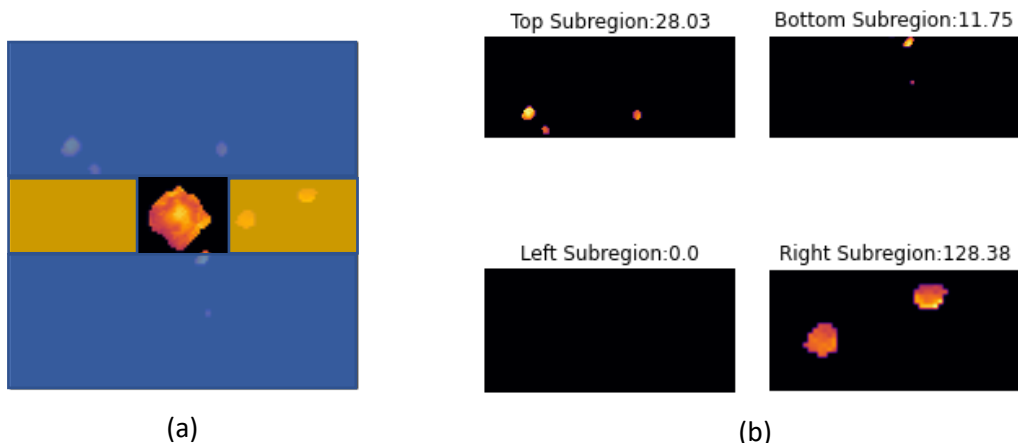


Figure 3.2.1 (a) Subregions from the original frame. (b) Subregions with their respective mean pixels intensity, to be added up as SRM measure of (a).

As shown in Figure 3.2.2, **PBP** metric is a measure of the proportion of bright pixels in the images. When the laser is off, PBP will have value which is close or equal to zero. Abnormally large coverage, for example plume, could be reflected as a spike in PBP.

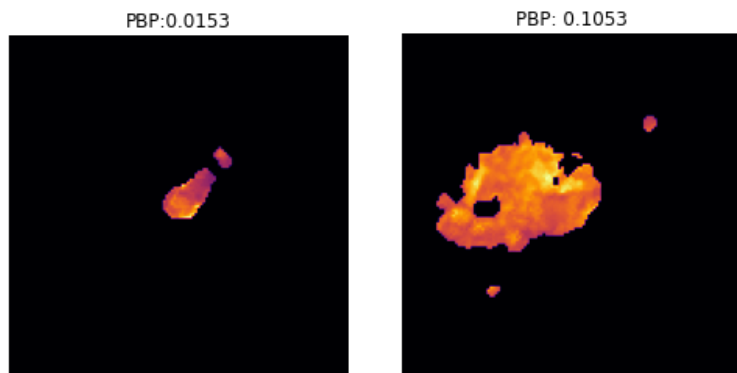


Figure 3.2.2 PBP metrics for melt pool frames with different proportion of bright pixels.

The **SD** metric changes according to the variation of melt pool's pixel intensity. It can be hypothesized that this metric captures some information about the spread of temperature field of the melt pool.

The computed metrics were standardised and plotted against the scan progress in the same plot as shown in Figure 3.2.3. There are some obvious varying patterns in the time evolution of these metrics. The global variations are due to the varying laser focus heights and the types of scans (border or straight scans) whereas local spikes mostly correspond to the video frames which contain anomalies. From Figure 3.2.3, metrics for melt pool images from block 4 and 6 are comparatively more stable.

The Pearson correlations between the metrics have also been computed and displayed in the form of heat map as shown in Figure 3.2.4. In general, large coverage of melt pool also means high scatteredness and wide spread of temperature field (correlation between PBP and the other 2 metrics are both greater than 0.80). Spread of temperature field is also positively correlated with the scatteredness of spatter particles although the correlation is comparatively lower (0.68).

Furthermore, by referencing on the positional dataset, as shown in Figure 3.2.5, the melt pools shortly before or after the turning points are sampled and visualized. The local heat transfer at these turning points are different, causing higher chance for the occurrence of anomalies and the formation of defects. Meander scanning strategy was employed for printing. Hence, it was expected to observe snapshots of turning melt pools.

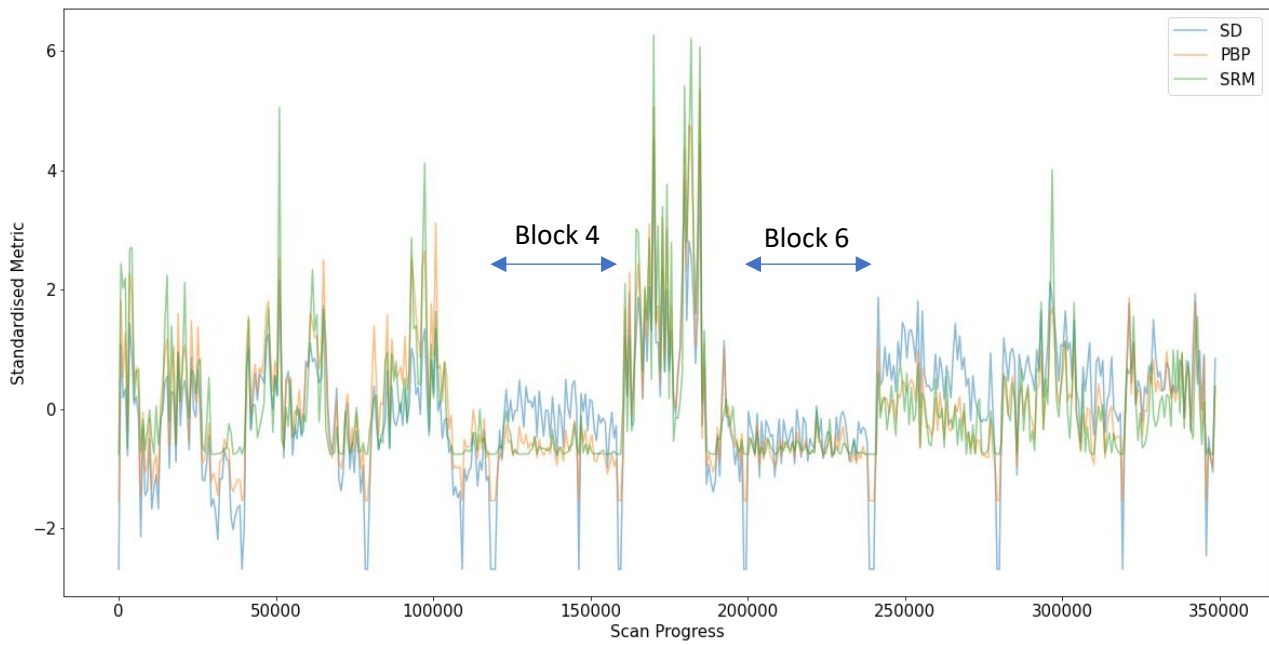


Figure 3.2.3 Change in standardised metrics along the scan progress.



Figure 3.2.4 Correlation heatmap for SD, PBP and SRM

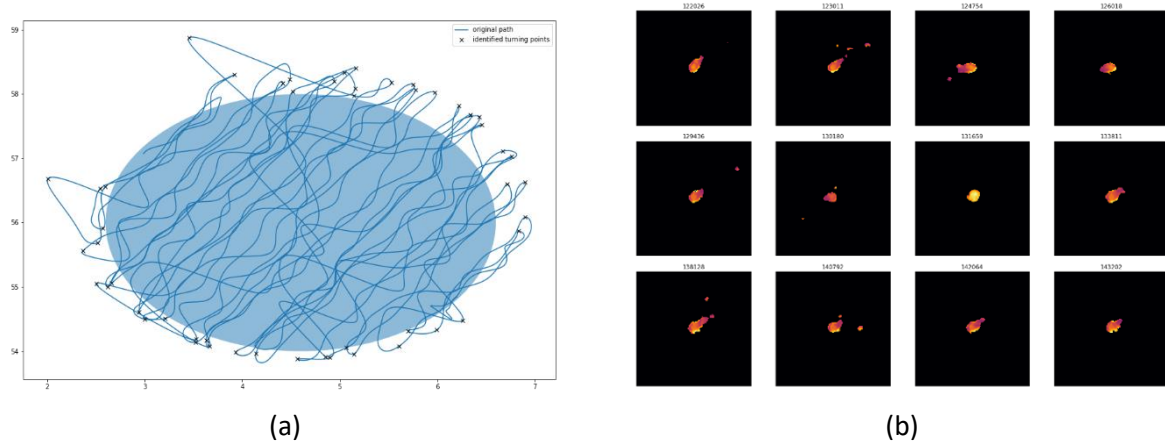


Figure 3.2.5 (a) Identified turning points outside of shaded regions and (b) melt pools sampled from turning points.

3.3 Region Properties Features Extraction

Clearly, the visualisation metrics serve as a coarse measure of melt pool dynamics. As an attempt to extract features which describe the dynamics of melt pool more precisely, a function from Python's Skimage module, "region props" was utilised for features extraction. The function was used to extract features such as average spatter area, blob (melt pool or plume) area, number of spatter particles, eccentricity of blob and eccentricity of spatter. Further inspection of average spatter area and blob area distributions (Figure 3.3.1 and Figure 3.3.2), block 4 and 6 with focus height 0mm and 4mm respectively give the cleanest melt pools. This agrees with the hypothesis developed during EDA. To determine the anomalous melt pools within these (mostly) clean melt pools samples, the combination of features needs to be considered.

Compared to the handcrafted metrics (SRM, PBP and SD), region props features provide a better description of the melt pool dynamics.

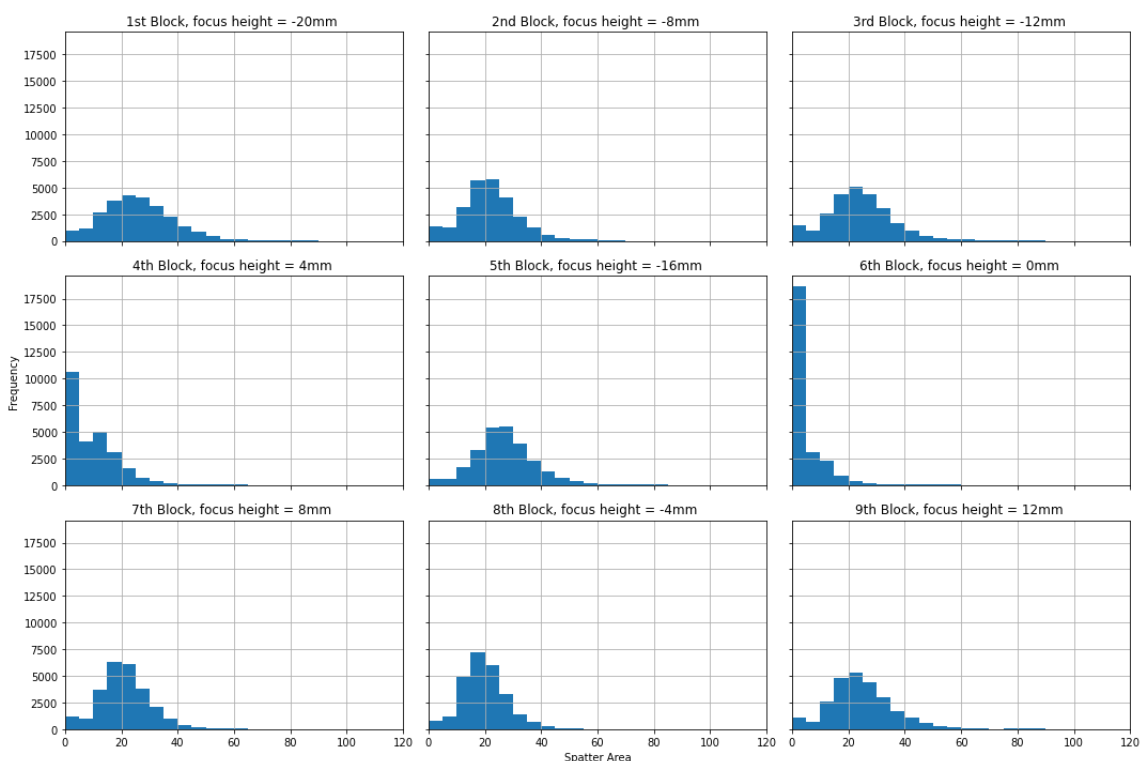


Figure 3.3.1 Average spatter particles area of melt pools produced under different focus heights.

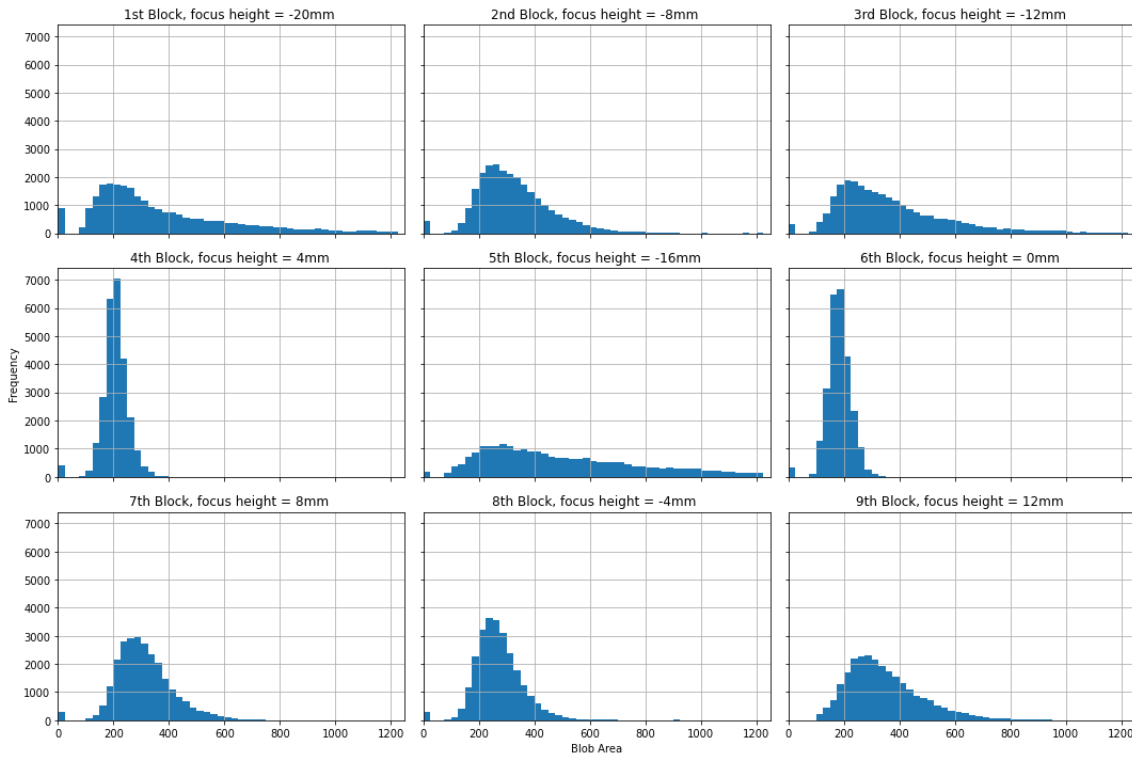


Figure 3.3.2 Blob size of various melt pools produced under various focus heights.

There are a few important things to note for the region props function:

1. The region props method is time consuming. On average, the processing time was $\sim 10^{-3}$ s per frame for features extraction. The frame per second (FPS) of test build 1 was 100k FPS, or equivalently successive frames have a time interval of 10^{-5} s. This means that if region props method is used for real time monitoring of LPBF process, the FPS of the coaxial monitoring system has to be ramped down (in this case by at least 100 times) to 1000 FPS.
2. In total, there are five features extracted, and one could explore the data to determine appropriate thresholds for anomaly detection. On the other hand, supervised machine learning models can be used an alternative to manually deciding the threshold. However, labelling melt pool frames is not an easy task as the decision boundary between a normal and anomalous melt pool can be very blur in some cases. Also, large amount of labelled data would be required for training, validation and testing purposes. With hard assignments of classes, there is also a lack of metric to quantify the degree of anomaly.
3. Currently, the set of features extracted might not necessarily provide a sufficiently good description for the state of melt pool for the purpose of anomalies detection. For example, there is no feature which capture the unstable tail scenario.

As such, following sections aim to resolve these identified issues.

4 One Class Learning Framework

To recap, there is a need to define a metric to measure the degree of anomaly for an in-situ monitoring system. Ideally, the evaluation of this metric should be computationally inexpensive such that it can be computed in near real-time setting. This section introduces an anomaly detection framework centred around the concept of one class learning. For demonstrative purposes, the examples shown entailed the framework applied on the older datasets (both build 2 and build3).

One class learning [26] is an unsupervised method of training classifiers when some classes in the dataset are either present in a small amount, or have no well-defined characteristics. The imbalanced dataset issue introduces overfitting risks as supervised machine learning models generally struggles to generalise for the class with lesser data. With one class learning, a classifier is trained to specialise in recognising well-characterised instances from a single class, hence this type of classifier is also known as a One Class Classifier. In the context of detecting anomalous melt pools, anomalies are not necessarily the minorities in the dataset, but they are not very well-characterised. This means that manually annotating the anomalies is prone to inconsistency error due to the less established definition of an anomaly (eg. How many spatter particles a melt pool must eject and how big must they be for the melt pool to be considered as an anomalous instance?). One class learning provides an alternative to supervised training as no labelling will be required for the training phase of the model.

There are a few examples of one class learning algorithms such as the autoencoder and one class support vector machine. In this project, the usage of a deep convolutional autoencoder is experimented for anomaly detection. The training dataset has to be pre-sieved for the removal of anomalies. This is to ensure that the autoencoder captures the underlying normal melt pools representations.

4.1 Data Filtering

This section presents a data filtering method for training data preparation. As mentioned, one class learning requires the anomalous instances to be the minorities in the training dataset. A quick way to achieve the required constraint is via the usage of unsupervised clustering algorithm such as k-means clustering.

The overall idea is to apply k-means clustering in the region props features space on printing datasets with focus heights of -4mm, 0mm, 4mm and 8mm. For convenience, melt pool dataset with focus heights of -4mm and 8mm are all labelled as “out-of-focus” while dataset with focus heights of 0mm and 4mm are labelled as “focused”. These labels will not be considered when computing

the distance in the clustering process -- they will only be used for proportion calculation in subsequent clusters analysis. Generally, the melt pool images in the “focused” dataset are comparatively focused and clean (normal) but there will still be anomalous instances within it. This is exactly the opposite case for the “out-of-focus” dataset. The goal here is to prepare a training dataset consists of normal melt pools from the “focused” dataset. K-means clustering employed on the region props features of this combined dataset will then group melt pool images which are similar together.

Having done with clustering, “focused” data points in clusters which best represent the “focused” dataset will be used for the training of the autoencoder. Such clusters would typically contain high proportion of “focused” data points and low proportion of “out-of-focus” data points. By doing so, all the features extracted via region props method were taken into account. More importantly, most anomalies originally in the “focused” dataset can be filtered out. An important assumption at this stage is that normal instances will be close to each other and anomalies will be scattered everywhere and far away from normal instances in the features space.

For clarity, k-means clustering’s implementation on build 2 and build 3 will be outlined as follow. Since the region props features are not on the same scale, they need to be standardised prior to k-means clustering. Next, the Elbow method [27] is used to determine the number of clusters. The optimal number of clusters is chosen to be 15, which is the first point where the decrease in sum-of-squared errors (SSE) is less than 5% as shown in Figure 4.1.1 (Build 2 data). To verify that k-means clustering behaves similarly across different builds, the melt pool images from the 3rd build are pre-processed and standardized in a similar way. From the bar plots in Figure 4.1.2, clusters 1 and 9 are consistently the two most imbalanced clusters with most data points from the “focused” category. Hence, it is safe to deduce that both clusters mostly captured the stable melt pools. This is also supported by the clusters’ centroid values (shown in Figure 4.1.3), where centroids of clusters 1 and 9 have zeros spatter properties, and the visualisation of melt pool images sampled from various clusters (shown in Figure 4.1.4). As for the remaining melt pools with “focused” label, they were considered as anomalies detected by k-means clustering.

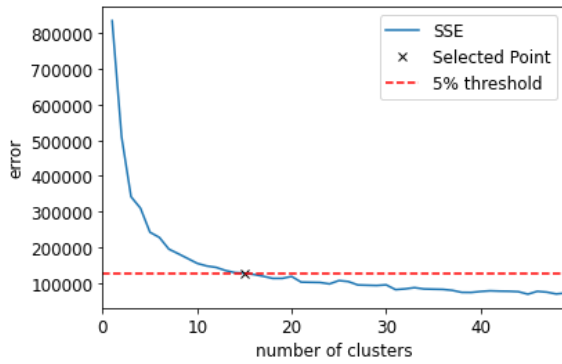


Figure 4.1.1 Elbow plot to for number of clusters selection

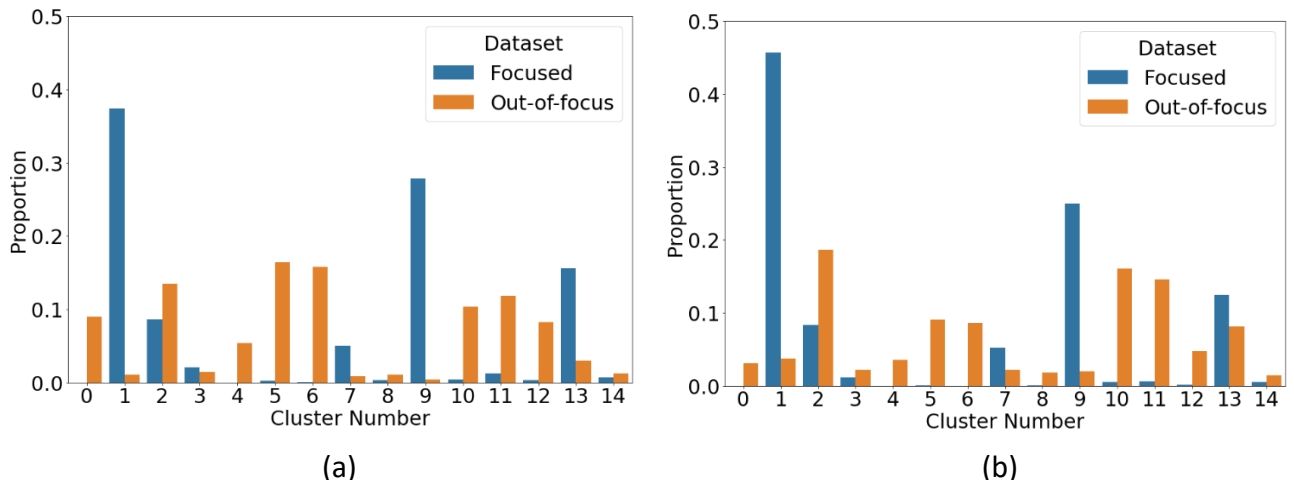


Figure 4.1.2 Proportion of “focused” and “out-of-focus” melt pools in each clusters for (a) Build 2 data (b) Build 3 data

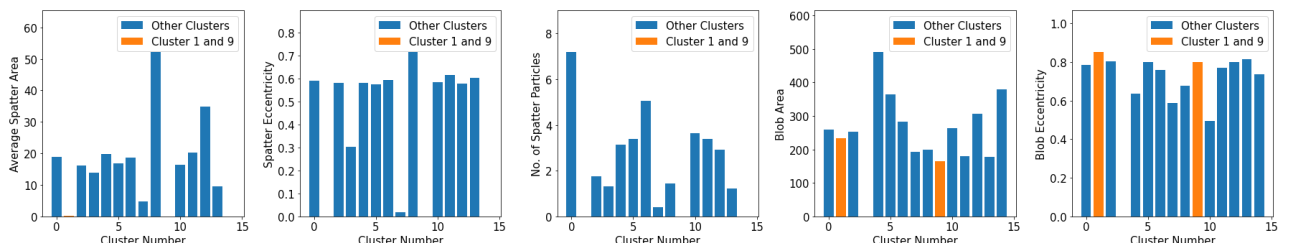


Figure 4.1.3 Bar plots for the clusters’ centroids (a) Average Spatter Area, (b) Average Spatter Eccentricity, (c) Number of spatter particles, (d) Blob area and(e) Blob Eccentricity of melt pools.

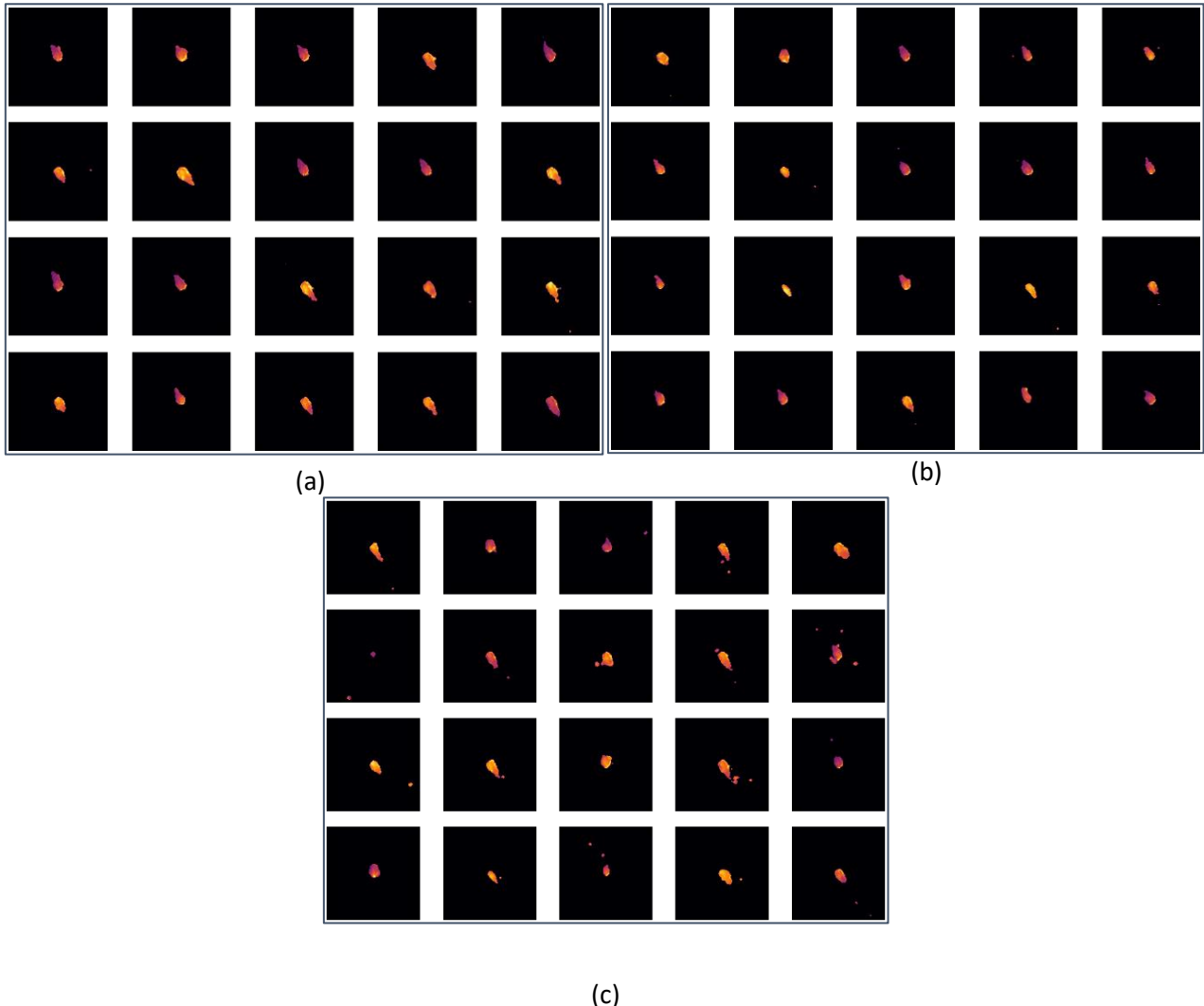


Figure 4.1.4 Melt pool frames sampled from (a) Cluster 1, (b) Cluster 9 and (c) Other clusters.

Based on Figure 4.1.2, most normal melt pools are concentrated within a few clusters, and that the remaining anomalies are distributed among all clusters. This suggests that the region props features described the “focused” melt pools similarly while “out-of-focus” melt pools are mostly scattered everywhere in the features space. This also fundamentally justifies the usage of one class learning framework for anomaly detection.

4.2 Autoencoder

Having obtained the training data, the next step is to train a one class classifier for anomaly detection purposes. A deep convolutional autoencoder is used as the anomaly detection model in this project. Deep learning models generalise by learning the underlying features automatically. For that reason, with the deployment of a sufficiently trained autoencoder, the coaxial monitoring system will not need to rely on any manual features extraction method for anomalies detection.

This section provides a brief introduction to an autoencoder. Figure 4.2.1 shows the generic architecture of an autoencoder. An autoencoder consists of two main components, the encoder and the decoder. The encoder compresses the high dimensional input data to a lower dimensional latent space, which is the bottleneck of an autoencoder's architecture. The decoder will then decode the encoding back to the original dimensional space. The process of encoding followed by decoding is subjected to the constraint where the decoder's output must be similar to the encoder's input. The decoder reconstructs the input data from the encoded information in the latent space. However, because of the smaller dimensional space in the bottleneck, the encoder is forced to only encode the most representative features from the input into the bottleneck to allow reconstruction of input data by the decoder. Deciding the dimension of the latent space is crucial as small dimensions will impose too much restriction on the flow of information from the encoder to the decoder, making it hard for the decoder to reconstruct the input data. On the other hand, with overly big latent dimensions, the encoder will not learn to capture the important features of the input data as not much restriction is imposed on the flow of information.

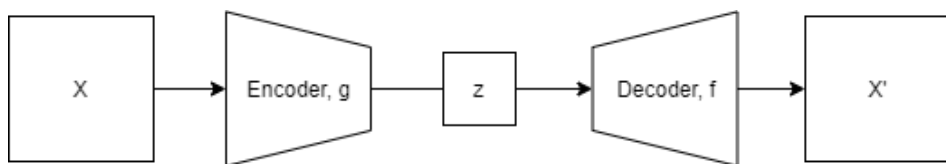


Figure 4.2.1 General architecture of an autoencoder.

Mathematically, this can be written as, $Z = g(X)$ and $X' = f(Z)$ subjected to $X \approx X'$, where X is the input image, g is the encoder, Z is the latent components, f is the decoder and X' is the output image. Equation (1) is the loss function of the autoencoder, \mathcal{L} . The loss function is used for the training of an autoencoder and it is the Euclidean distance between X and X' . The autoencoder aims to minimise the loss function during the training process so that the resulting output is similar to the input data.

$$\mathcal{L} = ||X - X'||^2 \quad (1)$$

The autoencoder used in this project has the architecture as shown in Figure 4.2.2.

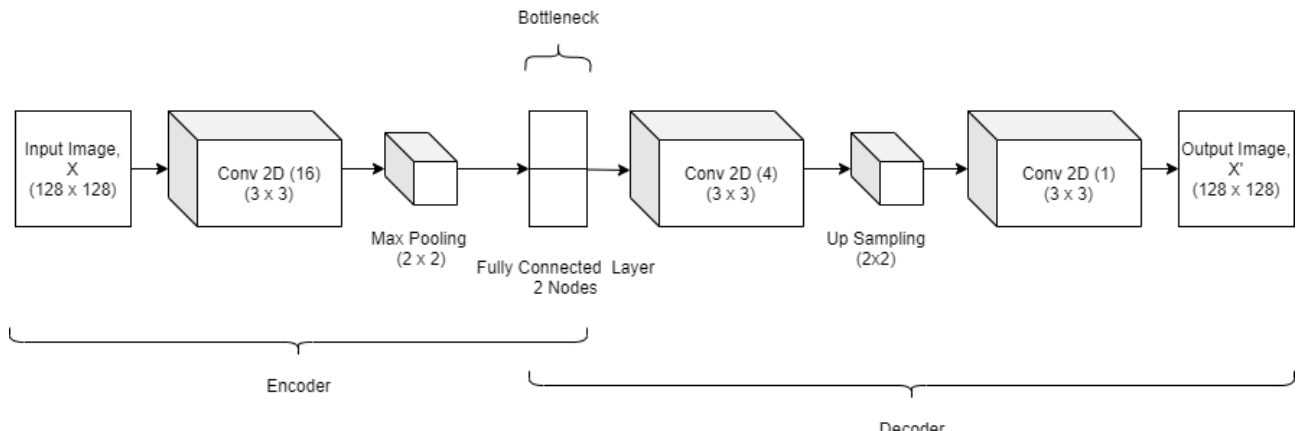


Figure 4.2.2 Architecture of the deep convolutional autoencoder used in this project.

With most anomalous instances filtered out from the training dataset, the autoencoder is trained to specialise in reconstructing normal instances of the melt pools. Prior to training, to ensure convergence in loss, min max normalisation is carried out so that the pixel values are all bounded between 0 and 1. The similarity measure between the input and output of images is the Euclidean distance between the images known as reconstruction error (RE). When a sufficiently trained autoencoder encounters an anomaly, it will not be able to reconstruct the anomalous image with high accuracy. This will translate to a high RE. Following that, the RE metric can be used to measure the degree of anomaly for any given melt pool frame.

4.3 Anomalies Detection

As a benchmark test, the RE metric of out-of-focus melt pool was computed and visualised on an interactive widget. As illustrated in Figure 4.3.1, the autoencoder fails to reconstruct encountered anomalies and that was reflected as spikes in the RE metric along the scanning process. The test also shows that, for out-of-focus printing, the RE provides a good relative measure for the degree of anomaly. For example, plume instance with larger coverage gives larger RE compared with smaller plume.

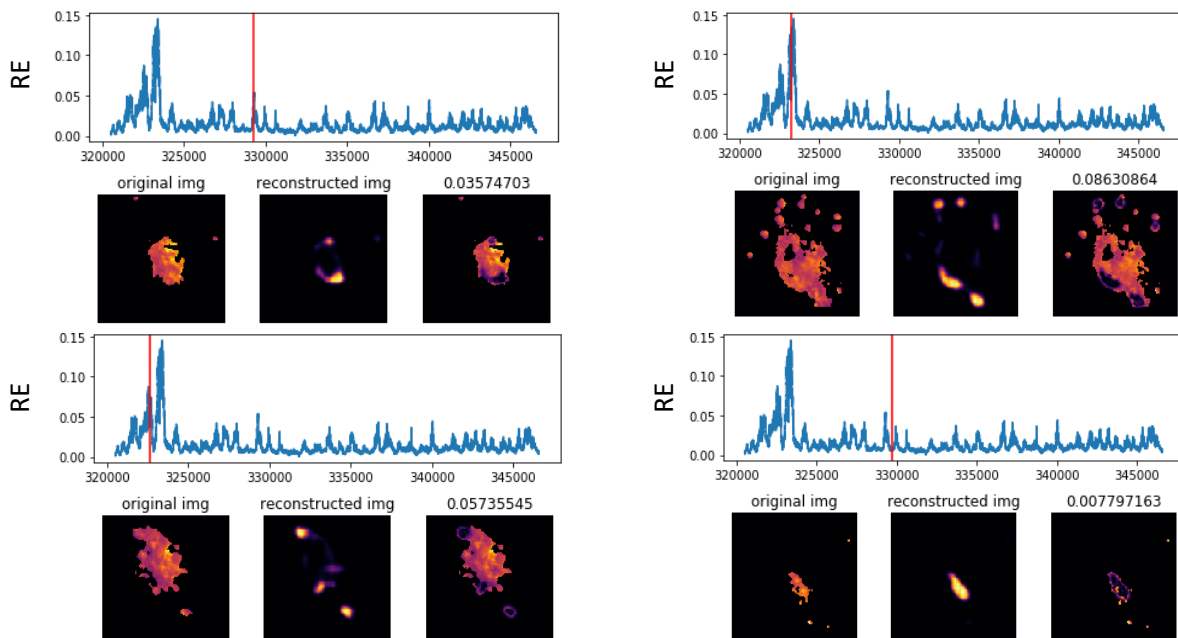


Figure 4.3.1 Benchmark test: Melt pools produced by scanning with focus height=-20mm

Next, the autoencoder is tested with focused melt pool images captured under optimised scan. This is to test for more representative printing situations, when printing parameters have been optimised but melt pool anomalies still occur unexpectedly. Firstly, the melt pools were sampled from different ranges of RE for visualisation. The sampled melt pool frames shown in Figure 4.3.2 illustrates that the RE metric generally worked for most cases. Melt pool images under focused scans seem to be increasingly unstable as RE increases. Some melt pools reconstructions are also presented for illustration in Figure 4.3.3.

To investigate the underlying melt pool features picked up by the autoencoder, the melt pool encodings at the bottleneck were computed. Since the latent vector is two dimensional, the melt pool encodings can be visualised in the form of 2D scatter plots. As shown in Figure 4.3.4 (a) and Figure 4.3.4 (b) are the scatter plots of latent vectors plotted with colour map to reflect the magnitude of RE. Figure 4.3.4 (c) and Figure 4.3.4 (d) show the scatter plots with anchored melt pool frames. There are two obvious clusters in the latent space, each capturing melt pools from one of

the opposing scan directions. It is worth noting that anomalies are still present in the dataset despite the data pre-sieving process. A remedy to this will be discussed in Section 4.4.

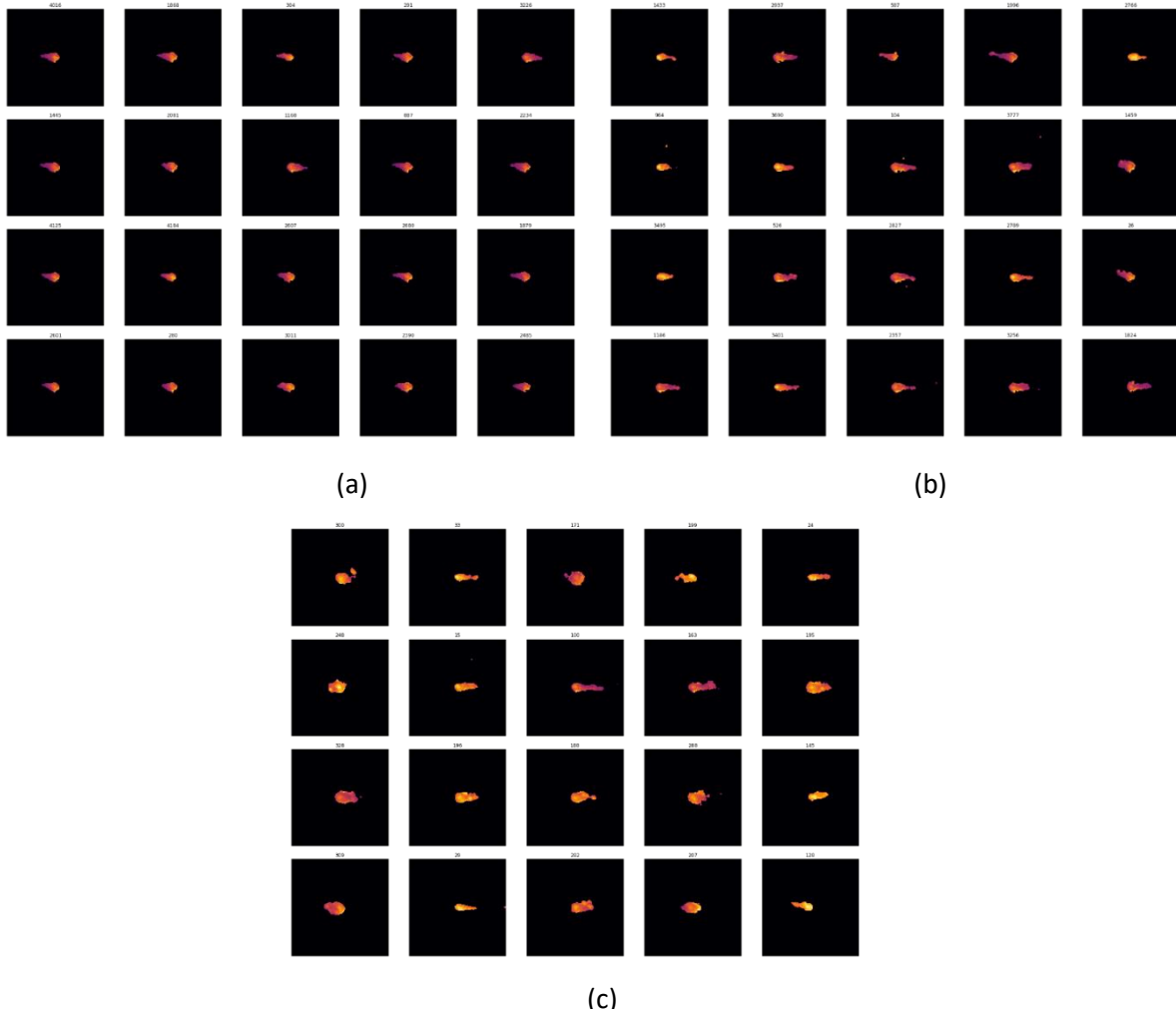
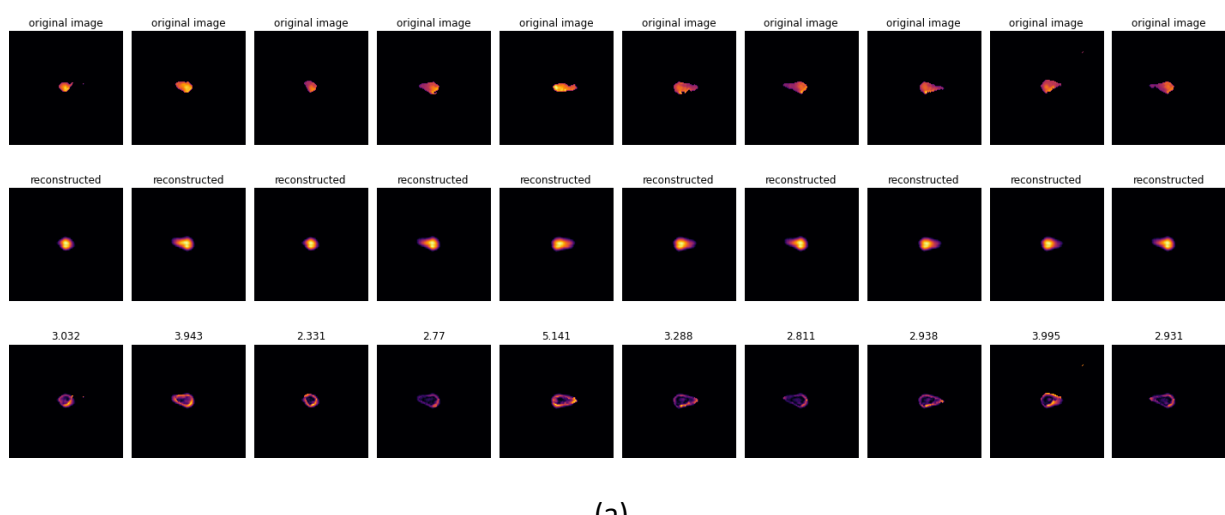
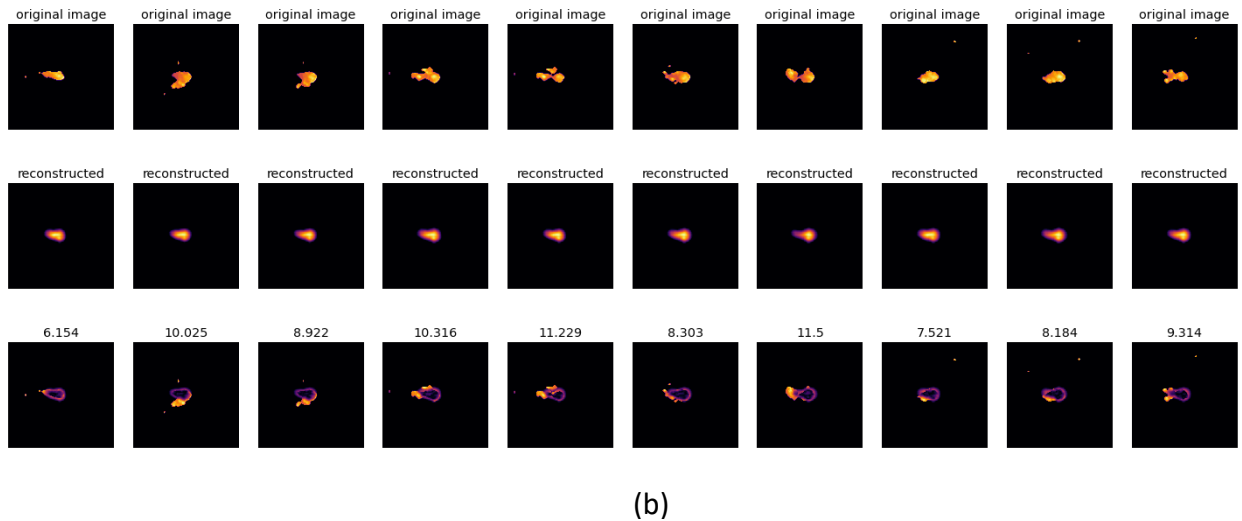


Figure 4.3.2 Melt pools sampled from (a) $RE < 0.003$ (b) $0.004 < RE < 0.005$ and (c) $RE > 0.006$



(a)



(b)

Figure 4.3.3 Original (first row), reconstructed (second row) and error melt pool images with RE $\times 10^3$ on top (third row) for (a) small RE (b) large RE.

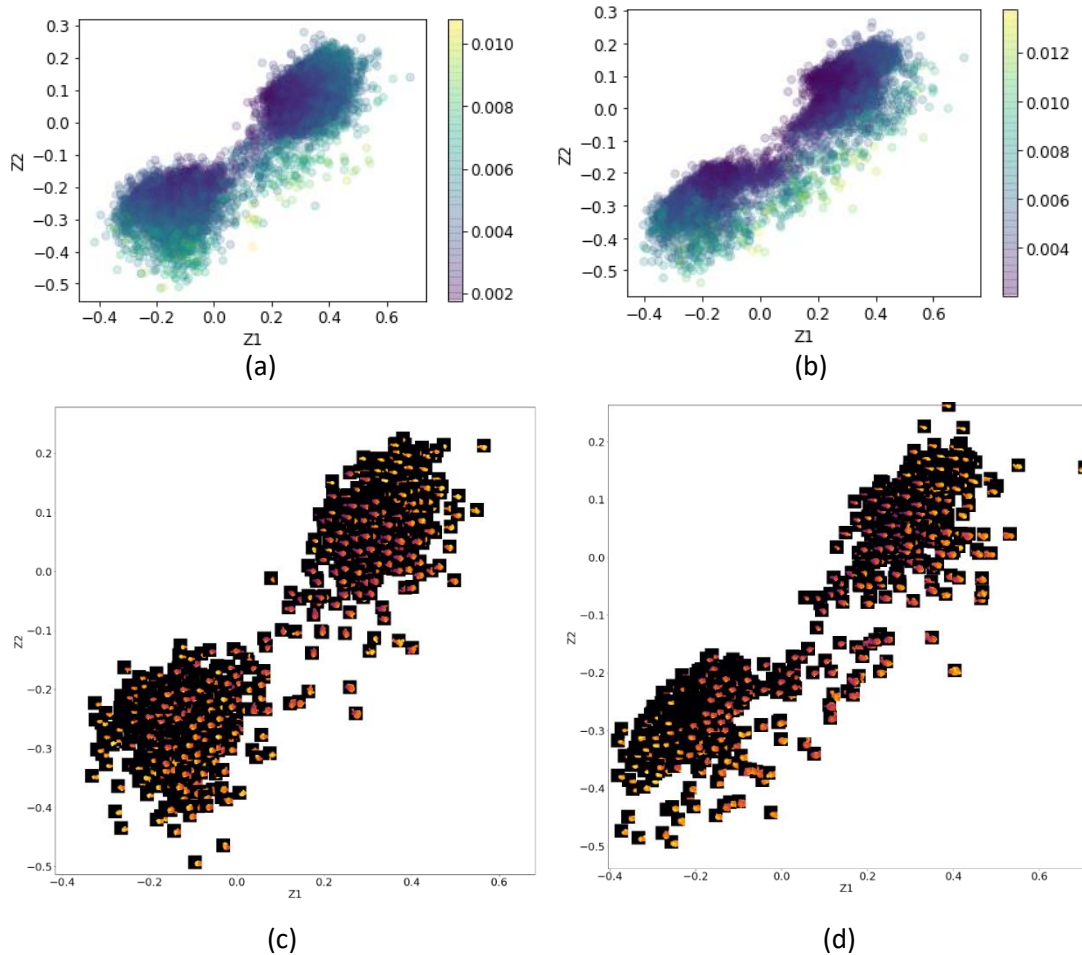


Figure 4.3.4 Scatter plot of the melt pool encodings for (a) Build 2 Training Data and (b) Build 2 Testing Data. Scatter plot with melt pool images anchored for (c) Build 2 Training Data and (d) Build 2 Testing Data.

4.4 Anomalies Detection Performance Evaluation

There are a few issues/ questions which may be raised at this stage:

1. What is the most appropriate RE threshold value that can be used to differentiate between a normal and anomalous melt pools?
2. Since k-means clustering algorithm was used prior to filter the dataset for the training of the autoencoder, naturally one might think that the autoencoder can only be as good as the k-means clustering algorithm for anomalies detection.
3. Some anomalies were escaped from the k-means clustering data pre-sieving algorithm.

To resolve these issues, it is necessary to introduce a method to evaluate the performance of the autoencoder and k-means clustering.

A receiver operating characteristic (ROC) curve [28] is a tool that can be used to visualise the performance of a classifier based on the trade-off between true positive rates and false positive rates. Typically, the vertical axis of a ROC curve represents a measure of the true positive rate (probability of detection) while the horizontal axis measures the false positive rate (probability of false calls). A typical ROC curve is shown in Figure 4.4.1. By adjusting the decision threshold of the classifier, one would be able to move along the ROC curve. Since the point $(0, 1)$ represents perfect classification, one point on the ROC curve is better than the other if it is to the northwest of the latter. To put things into context, for anomalies detection with the autoencoder, lowering the thresholding RE would result in more anomalies correctly identified but also an increase in the false alarm rate, thus moving along the ROC curve in the northeast direction. For exactly the opposite reason, increasing the thresholding RE will move along the ROC curve in the southwest direction. With the ROC curve, the performance of the autoencoder can now be evaluated and compared with that of k-means clustering.

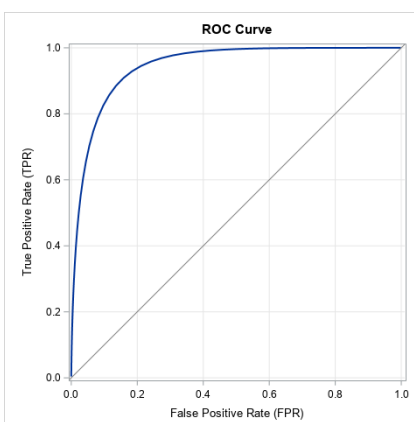


Figure 4.4.1 A typical ROC curve.

The first step is to determine the most appropriate RE threshold that differentiates between normal and anomalous melt pools. Melt pool dataset from the same build with focus height of 0mm and 4mm were split into training, validation and testing datasets. The training data was used for the k-means clustering data filtering method and then the training of the autoencoder following the methodology as described thus far. The melt pool frames in the validation and testing datasets were both annotated manually with classes such as “anomalous” and “normal”. Then, the trained autoencoder was employed on the validation dataset to determine an appropriate RE thresholding value with the usage of the ROC curve. Finally, the testing dataset was used to compared the performance of k-means clustering with that of the autoencoder. To recap, for k-means clustering, the melt pools which ended up in the highly imbalanced clusters are treated as normal melt pools and the remaining ones in other clusters are classified as anomalies. For the autoencoder, its performance will be based on the determined thresholding RE from the validation dataset. It is important to note that the testing dataset is an unseen but representative dataset to both the autoencoder and the k-means clustering model.

As a remedy to remove the anomalies present in the training dataset, a density-based clustering algorithm, DBSCAN was implemented as an additional layer of anomalies filter. It removes the anomalies which are located in the less packed region in the latent space, as shown in Figure 4.4.2. Then, the cleaned data was used to train a newly instantiated autoencoder. Subsequently, a new RE threshold can be determined from the same validation data.

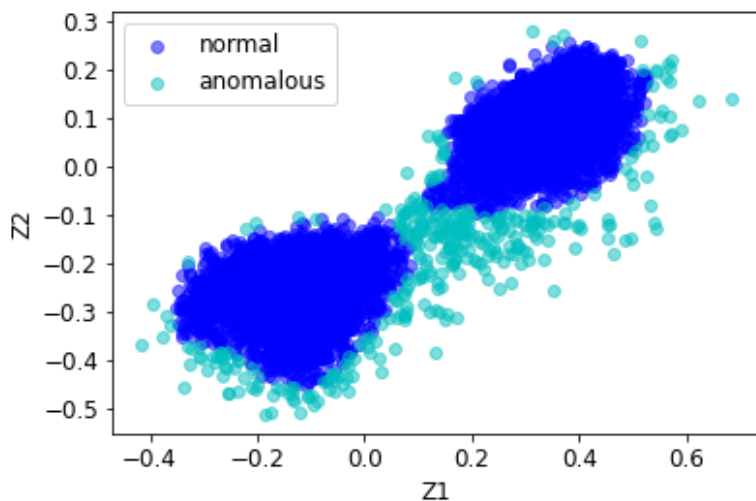


Figure 4.4.2 DBSCAN applied on latent space of Build 2 training data.

From the labelled validation data, ROC curves were used to determine the RE threshold as shown in Figure 4.4.3. The determined thresholds for autoencoder and autoencoder-DBSCAN

methodologies are also shown on the normalised histogram plots in figure. Finally, there are a few important insights one can draw from the performance metrics shown in Table 4.4.1:

1. Based on the recall metric for “anomalous” category, the ordinary autoencoder does perform better than the k-means clustering algorithm. Having a higher recall metric for “anomalous” category, it means that the former correctly predicts anomalous instances more frequently.
2. With further filtering by DBSCAN, the autoencoder improves its precision for anomalous cases although this also results in a small drop in “anomalous” recall.

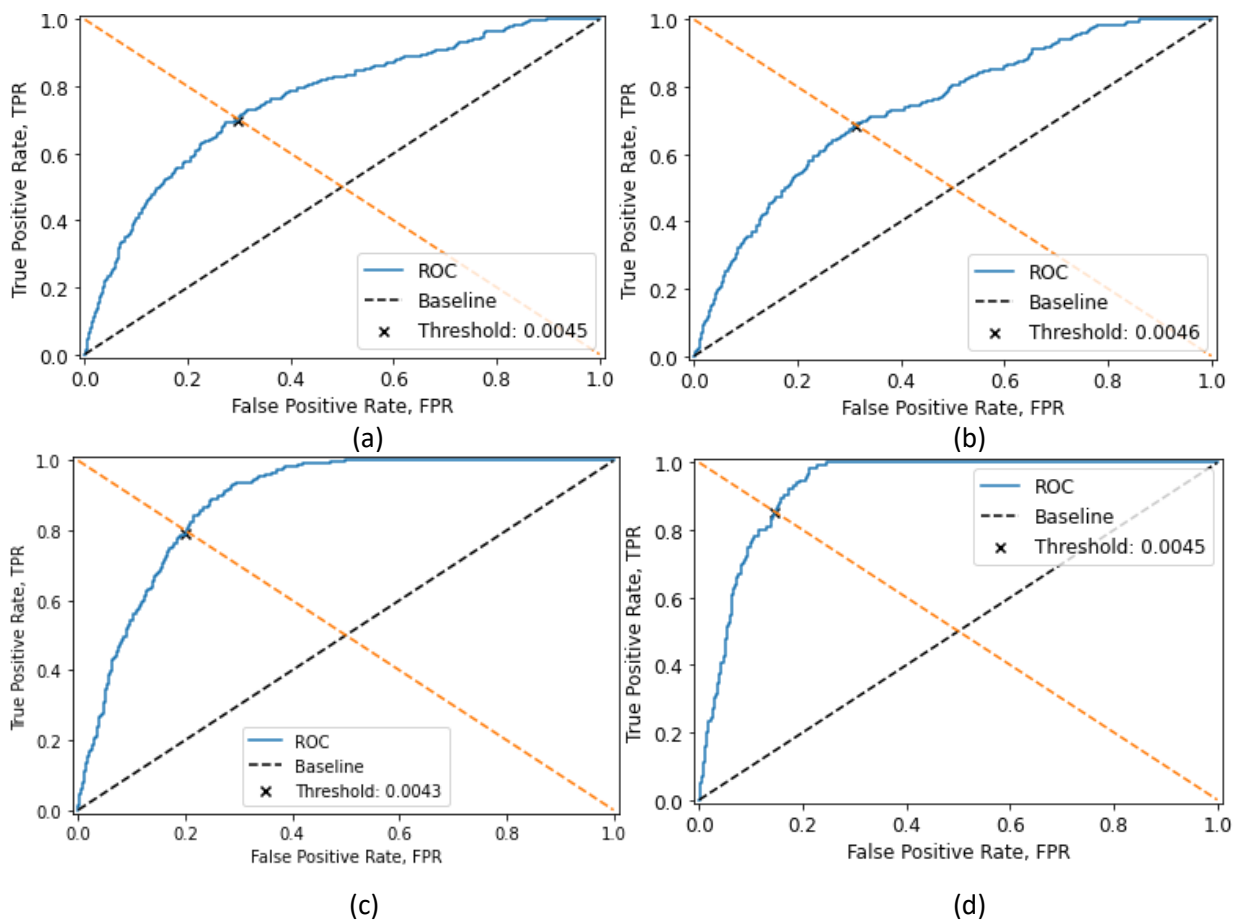


Figure 4.4.3 ROC curve for (a) Autoencoder applied on Build 2 Validation Data, (b) Autoencoder trained on data cleaned by DBSCAN applied on Build 2 Validation Data, (c) Autoencoder applied on Build 3 Validation Data and (d) Autoencoder trained on data cleaned by DBSCAN applied on Build 3 Validation Data

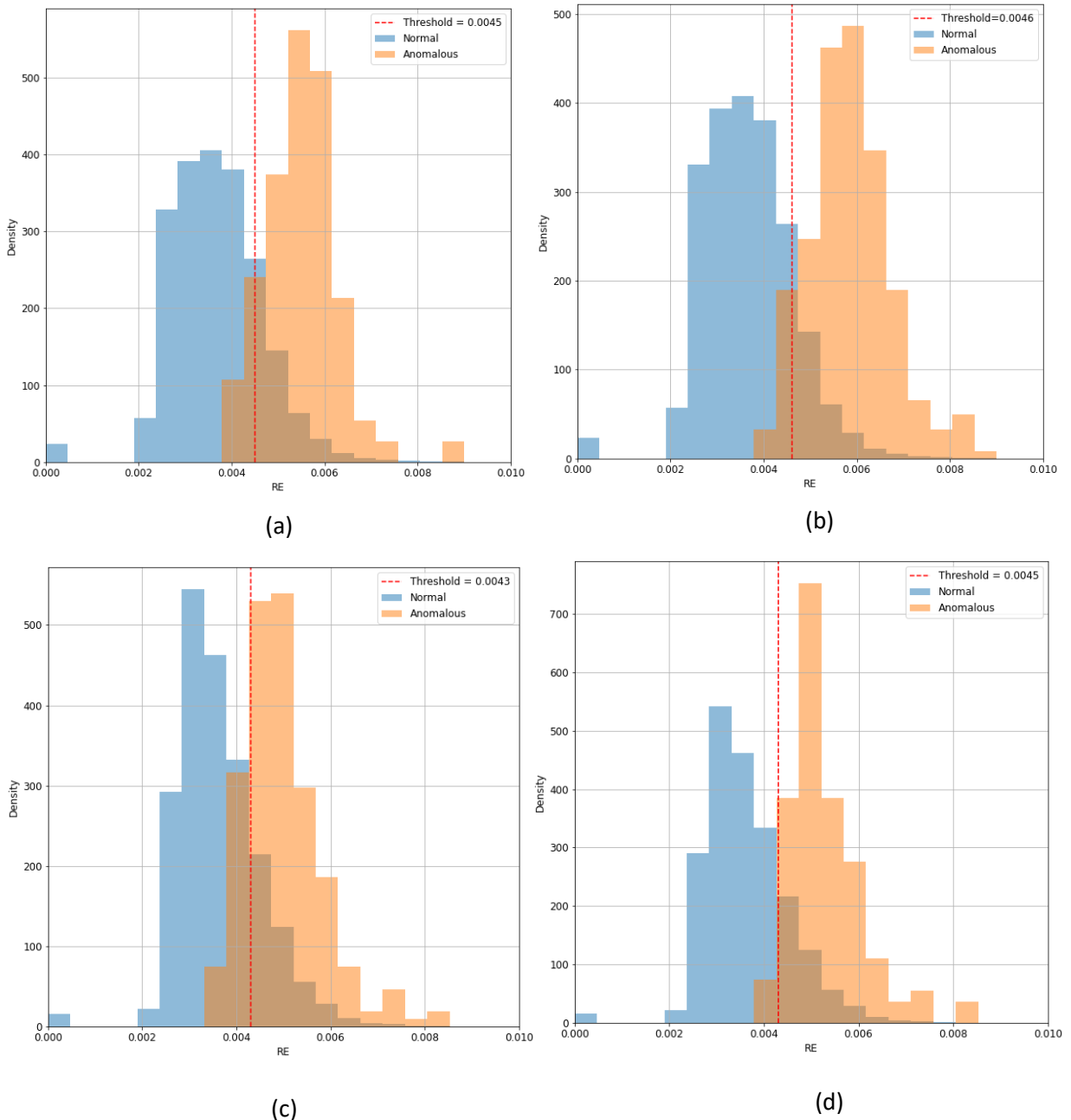


Figure 4.4.4 Normalised histogram for “Normal” and “Anomalous” instances for (a) Autoencoder applied on Build 2 Validation Data, (b) Autoencoder trained on data cleaned by DBSCAN applied on Build 2 Validation Data, (c) Autoencoder applied on Build 3 Validation Data and (d) Autoencoder trained on data cleaned by DBSCAN applied on Build 3 Validation Data

Table 4.4.1 Classification Performance of K-Means Clustering, Autoencoder and Autoencoder-DBSCAN

	Categories	Avg. Recall	Avg. Precision
K-Means Clustering	Normal	0.89	0.54
	Anomalous	0.29	0.73
Autoencoder without DBSCAN	Normal	0.71	0.96
	Anomalous	0.75	0.60
Autoencoder with DBSCAN	Normal	0.76	0.96
	Anomalous	0.76	0.71

4.5 Discussion of Framework

Measuring the time required for this anomaly detection framework, from min max normalising an image to RE computation, an autoencoder on average took $\sim 10^{-6}$ s to output a prediction. This is approximately 1000 times faster than region props features extraction alone. More importantly, the image processing is also faster than the FPS of LPBF in-situ monitoring system used. Also, being a completely unsupervised model, the training of the autoencoder does not require any manual labelling, this is a huge save in effort as supervised deep learning models typically need a lot of labelled data. Overall, the implementation of one class learning framework shows great computational time saving for LPBF in-situ monitoring. Example of usage could be helping the monitoring system to identify anomalies and selectively applying region props features extraction for subsequent melt pool anomaly analysis.

There are a few issues with one class learning framework involving autoencoder. Firstly, the performance of an autoencoder varies with different printing conditions. Data extrapolation is mostly an issue for machine learning models, however, since the autoencoder works by encoding the most informative features from the input data, the usage of it is even more data specific. This is good for the purpose of one class learning but the robustness of RE would be questionable for melt pool images produced under different printing parameters. For instance, an autoencoder trained with melt pools captured from a meander scanning would probably be bad at reconstructing most melt pool images from island scanning strategy, regardless of whether they are anomalous or not. Secondly, the RE metric, being a proportional measure of Euclidean distance in pixel space, measures the degree of anomaly but classification of anomalous melt pools is still needed for further investigation. An interesting approach for downstream anomalies classification task would be to

make use of the encoded latent vectors for classification since this compressed form of data contains the most valuable information about the melt pool geometries. Using the latent components as extracted features, classification of melt pools can then be carried out in a supervised manner. This will be illustrated in more details in subsequent Section 5. For this project, the RE computed from the autoencoder’s reconstruction will be used purely as a measure of anomaly together with region props features.

5 Automated Features Extraction Framework

The usage of an encoder provides a means of describing melt pool images with fewer parameters. Essentially, this is a form of data compression. However, as illustrated in Section 4.3 the latent vectors encoded by the autoencoder are highly-packed and appeared in clusters form. As a result, the latent space is not smooth and continuous. It is possible to resolve this with a variant of autoencoder to better describe the melt pool geometry. This section presents an automated features extraction methodology for anomalous melt pool detection and classification tasks centred around the usage of a disentangled variational autoencoder (β -VAE). Specifically, the data compressing property of the variational autoencoder will be used for the extraction of melt pool representations. To demonstrate the workflow, the data processing results from new Build 3 dataset will be shown in this section.

5.1 Data Pre-processing

With the goal to describe the melt pool geometries in a more precise manner, the melt pool images are cropped from a size of 128x128 into 32x32. This is because the melt pool's surrounding does not contain much information about its geometry.

To retain the coaxial point of view, the melt pool has to be contained within the cropped region. Firstly, the centroid of a melt pool is obtained with the region props functionality. Then, the image is cropped into a size of 32x32 with the melt pool's centroid being the centre of the cropped image as shown in Figure 5.1.1.

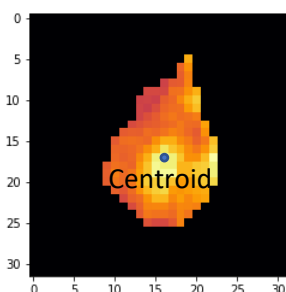


Figure 5.1.1 Cropped image of melt pool with a size of 32 x 32 and centroid of the melt pool aligned with the centre of the image.

Next, min max normalisation is carried out on the cropped image. Unlike the one class learning framework, this framework does not rely on any profiling for the normal melt pool. Hence, the data does not need to be pre-sieved.

5.2 Disentangled Variational Autoencoder (β -VAE)

This section provides an overview of a variational autoencoder (VAE). A VAE has a similar structure as an autoencoder, except that it is a probabilistic variant of the latter. The usage of a VAE assumes that there are several unobserved data generating factors (also known as representations), each controlling different aspect(s) of the input. Following that, the goal here is to train a VAE to approximate the representations' distributions so that the encoder can effectively be as a features extractor. Figure 5.2.1 shows the structure of a generic VAE, where the probabilistic encoder, $q_\phi(z|x)$ maps the input data X to a latent vector $z = \mu + \epsilon \odot \sigma$ where ϵ is the distribution mean, σ is the distribution standard deviation and the stochastic $\epsilon \sim N(0, 1)$. On the other hand, the decoder $p_\theta(x|z)$ maps any sampled vectors from the latent space back into the original dimension.

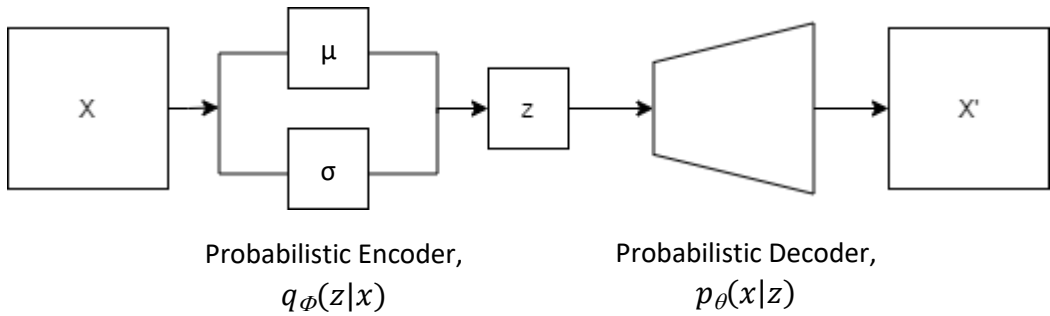


Figure 5.2.1 Generic architecture of a variational autoencoder

$$\mathcal{L}(\theta, \Phi; x) = -E_z[\log p_\theta(x|z)] + D_{KL}(q_\phi(z|x)||p_\theta(z)) \quad (2)$$

Equation (2) represents the loss function of a typical VAE. This loss function has two terms in it. The reconstruction loss, $-E_z[p_\theta(x|z)]$ ensures that the reconstructed data is similar to the input. The second term, also known as the KL-divergence term is a measure of the difference between $q_\phi(z|x)$ distribution and the prior distribution of the latent encoding, $p_\theta(z)$. It imposes a penalty to the network when it encodes the input into a highly-packed region, thus encouraging the encodings to acquire a distribution similar to that of $p_\theta(z)$, which is assumed to be $\sim N(0, I)$. Minimising this loss function during the training process is equivalent to maximising the lower bound of the data log likelihood, $p(x)$ also known as evidence lower bound (ELBO) [29]. By assigning a relative weightage, β to the loss terms in Equation 2, the loss function of a disentangled variational autoencoder (β -VAE) is obtained as in Equation 3,

$$\mathcal{L}(\theta, \Phi; x) = -E_z[\log p_\theta(x|z)] + \beta * D_{KL}(q_\phi(z|x)||p_\theta(z)), \quad \beta \geq 0 \quad (3)$$

The modification of this loss function allows control of the amount of disentanglement between the encoded latent components. A set of latent components is said to be disentangled when each component is relatively sensitive to changes in a single aspect of the representations while being insensitive to the others. According to [29], β introduces a pressure on the encoder to reduce redundancy in encodings, causing the latent components to be less correlated with each other. In the context of melt pool geometry, when the latent encodings are perfectly disentangled, varying one latent component will only change an aspect of the melt pool geometry. Whereas for normal VAE ($\beta = 1$), it is difficult to understand which aspect of the melt pool geometry is captured by each individual latent component, as varying one latent component results in changing in multiple aspects of the melt pool geometry.

In this project, the β -VAE architecture employed has an architecture as shown in Figure 5.2.1.

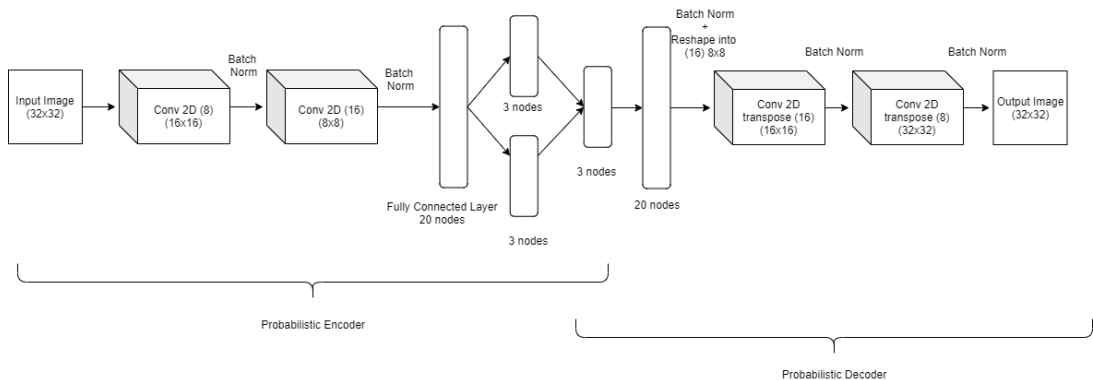


Figure 5.2.1 The architecture of the β -VAE used in this project.

5.3 Features Extraction

By training a β -VAE on build 3's data, the encoder learns the probability distribution of the melt pool latent representations. To explore the encodings, one could sample from specified ranges in the latent dimensions and decode the sampled latent vectors for visualisation. Figure 5.3.2 aims to illustrate how melt pool geometry changes with the latent components. With a $\beta = 4$, the encodings showed some level of disentanglement. Based on Figure 5.3.2, the first (Z1), second (Z2) and third (Z3) components of the melt pool represents different aspects of the melt pool geometries such as the size, roundness and tail length (and also tail direction). Upon closer investigation, in Figure 5.3.2(c), it appears that the encoder has also learned to encode the tail separation phenomena. The distributions of the first two latent components shown in Figure 5.3.3 resemble closely to a gaussian distribution with zero mean and unity standard deviation. This is a result of weighting the KL divergence term in the loss function. Also, Z3 exhibits a bimodal distribution since it captures the melt pool tail length and direction as shown in Figure 5.3.2(a). This bimodal

distribution is expected since the proportion of melt pools travelling in both directions should be roughly equal for a meander scanning strategy.

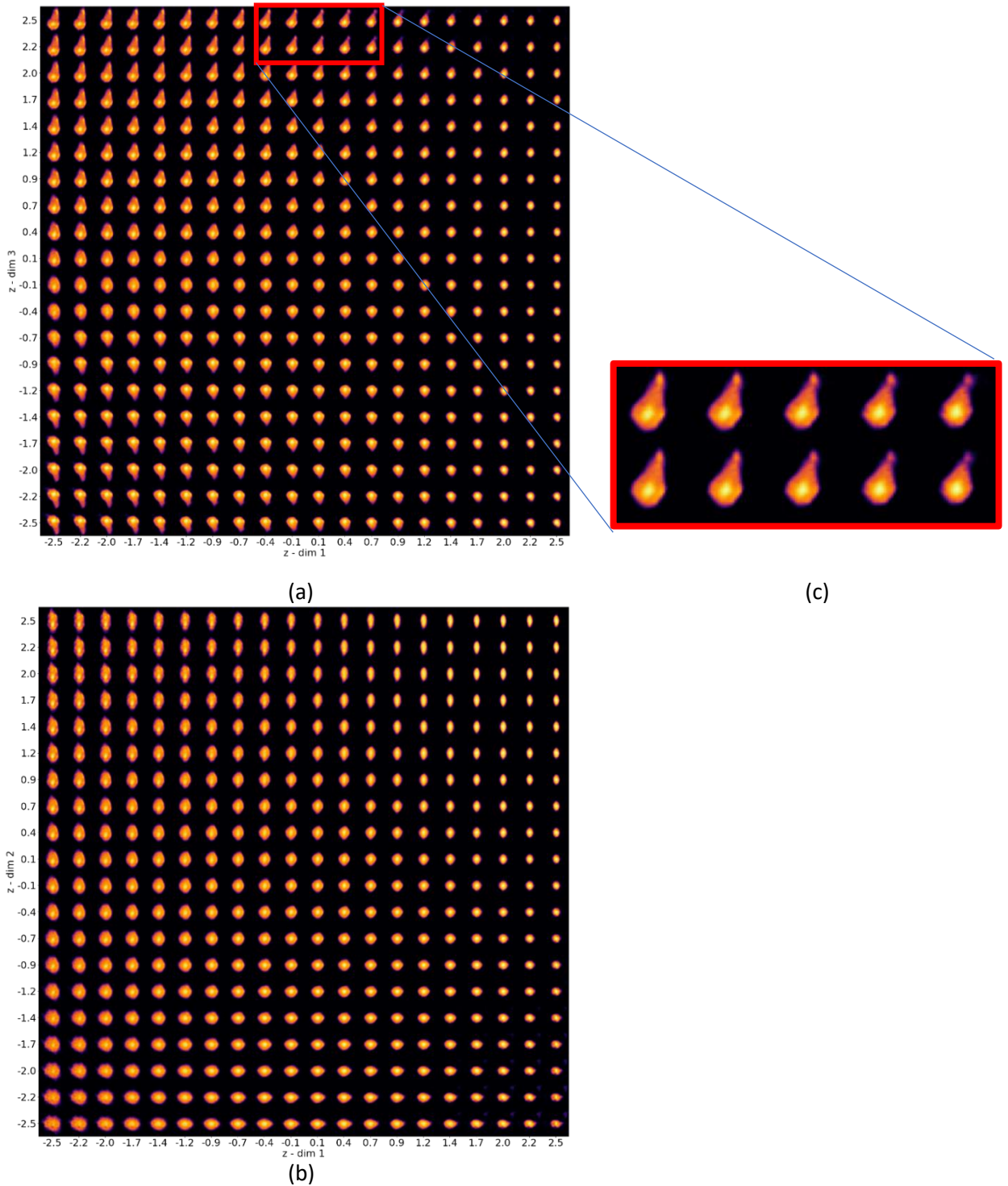


Figure 5.3.2 Grid plots of generated melt pool results (a) Z_3 against Z_1 with $Z_2 = 0$, (b) Z_2 against Z_1 with $Z_3 = 0$. (c) Tail separation phenomena captured by the β -VAE model.

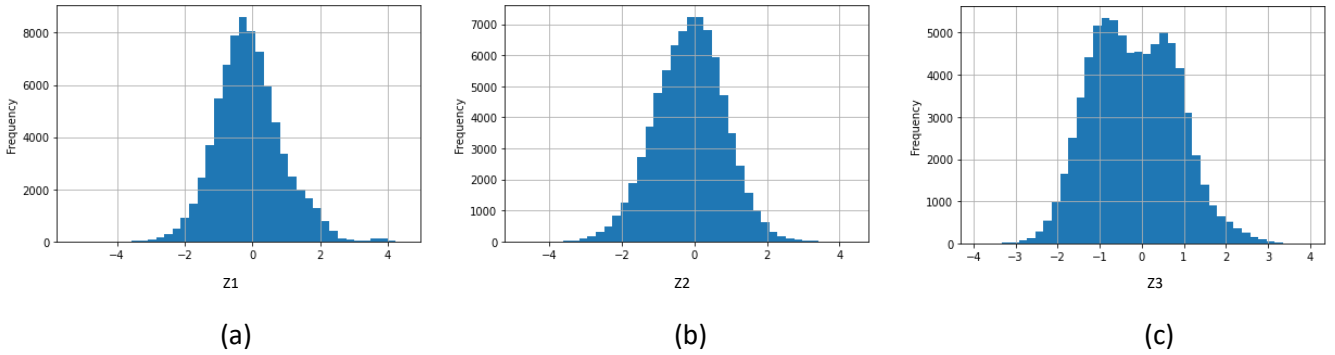


Figure 5.3.3 The distributions of latent components (a) Z1, (b) Z2 and (c) Z3.

5.4 Anomalies Detection

Next, the encoded melt pools are presented in the form of scatter plots as illustrated in Figure 5.4.1. Based on the scatter plots, the encodings seem to agree qualitatively with the latent representations visualised in Figure 5.3.2. Besides, several anomalies are encoded relatively far away from the dense region in the latent space. This suggests the usage of Euclidean Distance metric from some reference point(s) as an anomaly measure. Based on the visualisation, it is also sensible to categorise the datapoints into clusters. Following that, the distance of melt pools from their cluster's centroid can be computed and used as the anomaly metric. Conceptually, this means that the more a given set of melt pool characteristics deviates from their average values the more anomalous the melt pool is.

As shown in Figure 5.4.2 are the scatter plots of data points in the 3D latent space. Prior to obtaining the distance metric, the outliers in Figure 5.4.2(a) were removed with DBSCAN as illustrated in Figure 5.4.2(b). This is to avoid the outliers to affect the computation of clusters' centroid. Then, k-means clustering algorithm was fitted on the cleaned data to obtain the centroids (Figure 5.4.2 (c)). It is appropriate to specify the number of clusters as two since Z3 exhibits a bimodal distribution and that it is sensible to compare images of melt pools travelling in the same direction. Having obtained the centroids, the distance of data points from their respective centroid can then be calculated and used as the anomaly metric as shown in Figure 5.4.2 (d).

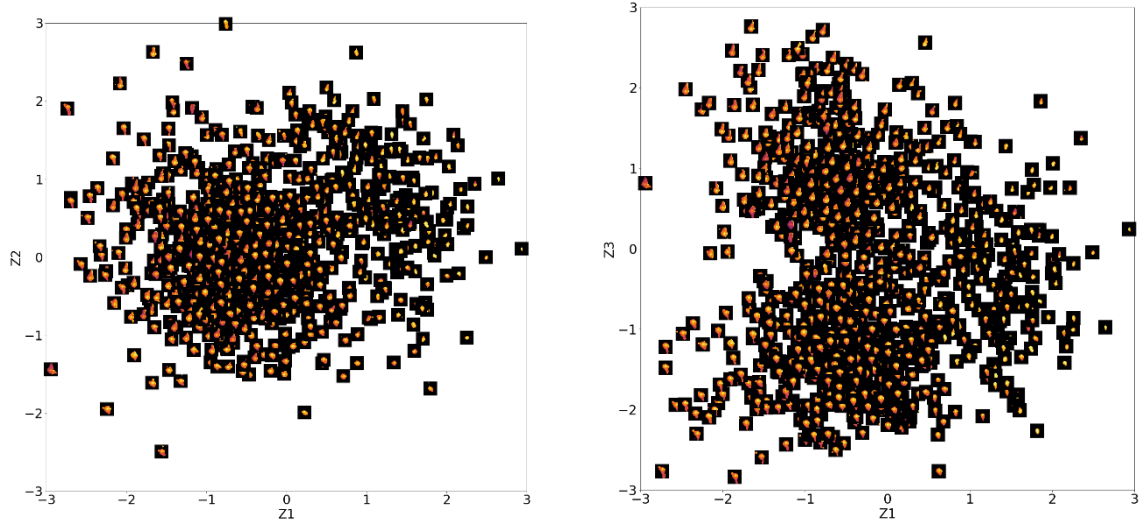


Figure 5.4.1 Scatter plots (with melt pool frames anchored) of the latent components for (a) Z2 against Z1 and (b) Z3 against Z1.

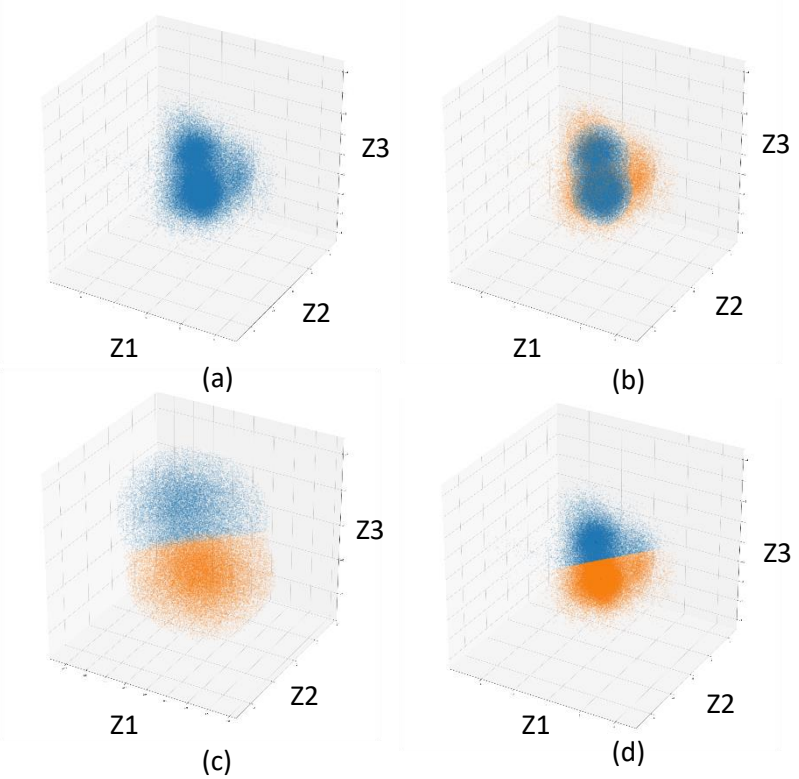


Figure 5.4.2 Scatter plots of (a) all the data points, (b) outliers (in orange) identified by DBSCAN and normal data points (in blue), (c) K-Means Clustering fitted on the normal data points and (d) all data points and the two identified clusters.

5.5 Anomalies Classification Performance Evaluation

Each representation captured by the β -VAE describes a different aspect of the melt pool geometry. Consequently, they contain information which is essential for the classification of melt pools. For melt pool classifications, a supervised approach was employed. The melt pool categories were decided based on observable melt pool geometries. For example, build 3 data contains “stable”, “unstable tail”, “long”, “large” and “plume” categories. Following that, 1500 images of melt pools were labelled and the annotated dataset was split into training (85% by proportion) and testing datasets (15% by proportion).

Three different supervised classifiers, Support Vector Machine (SVM), K-Nearest Neighbours (KNN) and Random Forest (RF) and are used for the melt pool anomalies classification task. The optimal hyperparameters for the classifiers were obtained with grid search cross validation with five folds. Finally, the testing dataset was used to quantify the performance of the classifiers. The classification results are summarised in Figure 5.5.1.

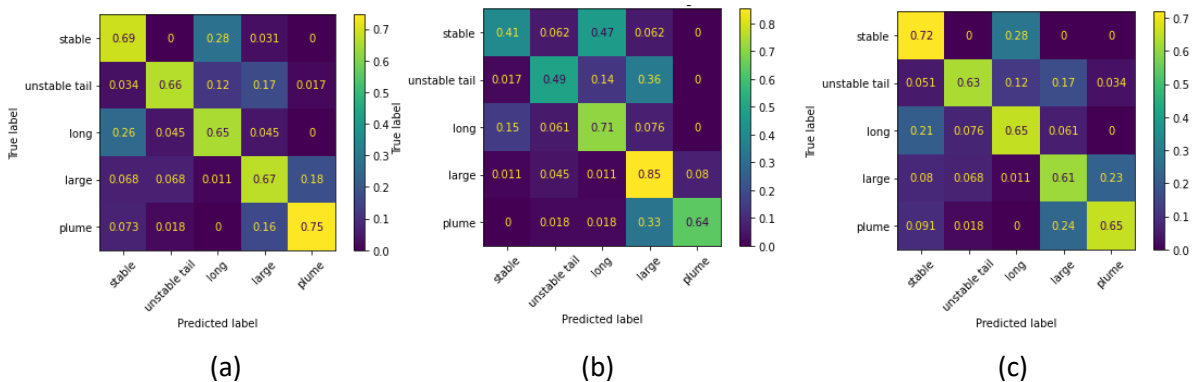


Figure 5.5.1 Confusion Matrix for Build 3 data classifications results. Focus height = 0mm
(a)SVM, (b)KNN and (c)RF.

For illustrations, the correct melt pool anomalies classifications for Build 3 are shown in Figure 5.5.2 respectively.

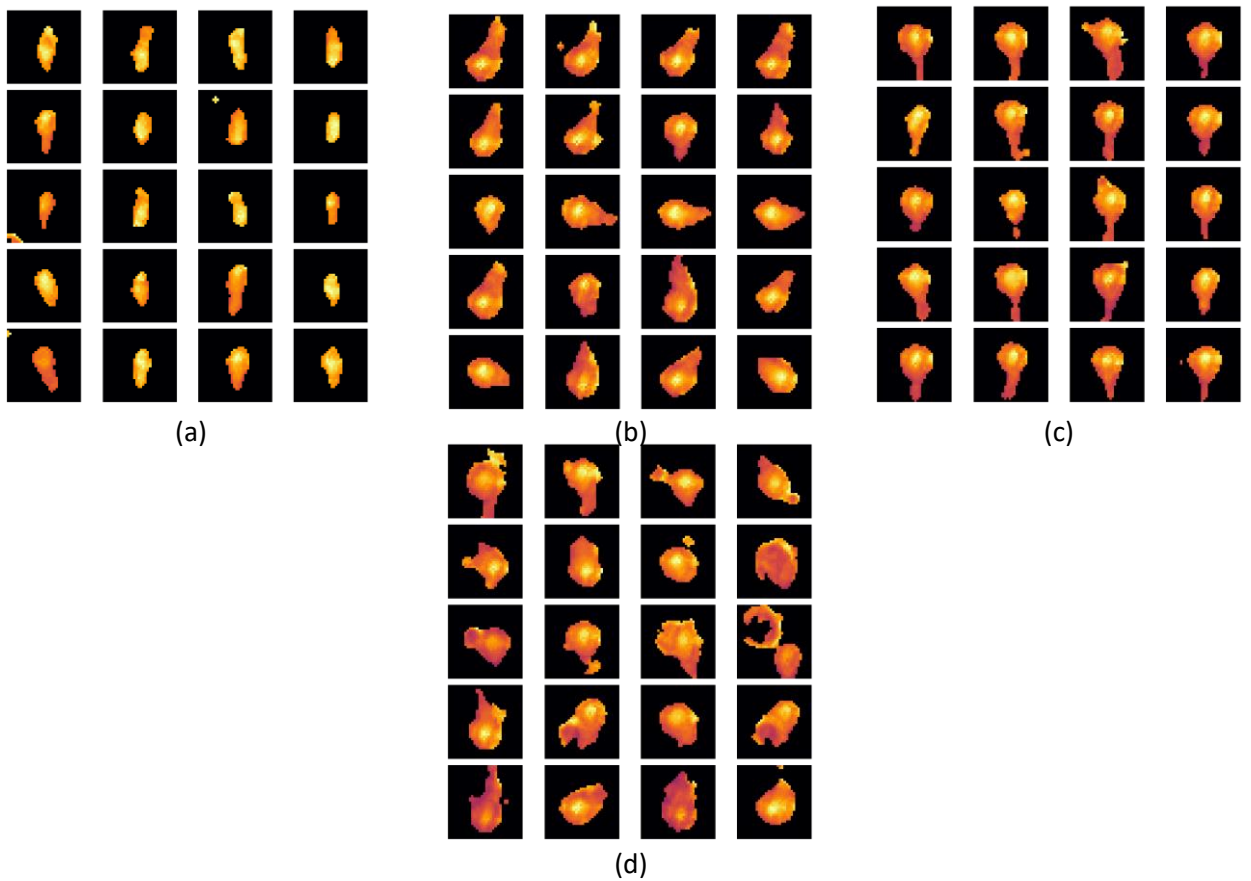


Figure 5.5.2 Build 3 correct classifications. (a) Long, (b) Large, (c) Unstable tail and (d) Plume.

5.6 Discussion of Framework

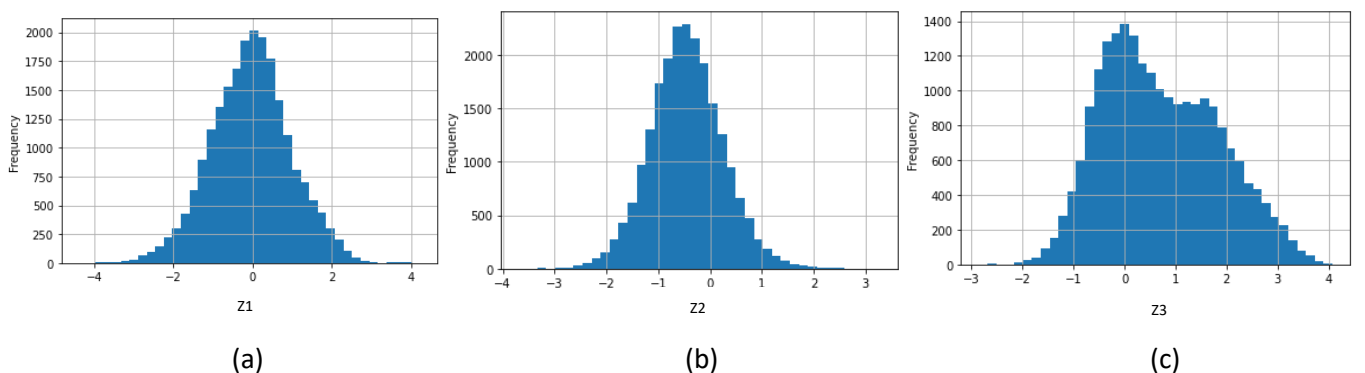


Figure 5.5.1 Latent components (a)Z1, (b) Z2 and (c) Z3 distributions as a result of unrepresentative testing dataset. (Train β -VAE on Build 3 test on build 2)

The β -VAE learns representative features of the melt pools. As for now, the model's descriptive capability is limited to dataset generated from similar printing parameters for example focus heights

and melt pool orientations. For instance, employing a β -VAE trained on Build 3 dataset on Build 2 melt pool images results in the distributions as shown in Figure 5.5.1, the relatively poor encodings especially Z3 can be attributed to both builds having different melt pool orientations. If compared to Figure 5.3.3, Z1 distribution is slightly distorted, Z2 experiences a slight shift in the entire distribution and Z3 becomes way less bimodal. A potential solution is to include data with more variation, for example melt pools from variety of optimised scans. With sufficient training and known limitations, the β -VAE can then generalise and cope for melt pool images produced from a wider range of scanning parameters.

It is also possible that the encoder wrongly recognised snapshot of spatter particles at the point of leaving the melt pool as the melt pool's tail causing it to mistakenly encode the direction of melt pool. Nevertheless, the classifiers trained on melt pools features encoded by β -VAE do show some promising results.

Finally, some caveats related to data processing. Anomalies, due to their stochastic nature, can have very different shapes and sizes. In fact, even with human's judgement assigning just one label to an anomaly instance can be a non-trivial task. For example, some cases of unstable melt pool tail can be similar to stable melt pool. This issue might be the bottleneck for the improvement of classifiers' performance. To resolve this issue, future work may explore on analysing the change of melt pool geometries across successive frames to enhance the classification results. Besides, multi labels assignment to a single frame can also be experimented. Some misclassifications are shown in Figure 5.6.2 further suggesting the difficulties in separating some classes with a single label assignment. In this project, the size of the cropped image was chosen to be 32x32 as most of the melt pools are able to fit into this size. For other builds, melt pools with large coverage, for example plume instance, may not be able to completely fit into the cropped region.



Figure 5.6.2 Misclassification results (a) "Unstable tail" predicted as "long" and (b) "Unstable tail" predicted as "Large"

6 Results and Discussions

A case study was carried out on the new Build 2 Dataset. The dataset corresponds to multilayer printing of LPBF build shot at 25K FPS. Aside from the melt pool frames and corresponding cartesian positional dataset, the surface microscopic image and depth measurement data for the topmost layer (L190) were also provided. This allow the investigation for the relationship between the occurrence of melt pool anomalies and surface defects formed during the printing process.

6.1 Methods

To relate the formation of defects on the printed builds, both frameworks discussed thus far have to be applied on this dataset. This section discussed about the data preparation process and the modifications that were done to suit for the training of models.

In the new dataset, it was observed that the melt pool frames mostly contain spatter particles. Furthermore, there was no melt pool dataset with 0mm focus height. As a result, the data pre-sieving step as outlined in Section 4.1 cannot be carried out. A decision was made to employ the autoencoder trained on previous the new Build 3 dataset (for the layer with with 0mm focus height) on the new dataset. Since the orientation of the melt pools are different (refer to Figure 6.1.1), prior to anomaly detection, the melt pools are rotated so that they are aligned vertically. This is to ensure the representativeness of the training dataset especially when the autoencoder reconstructs the melt pools based on their orientation as depicted in Figure 4.3.4 in Section 4.

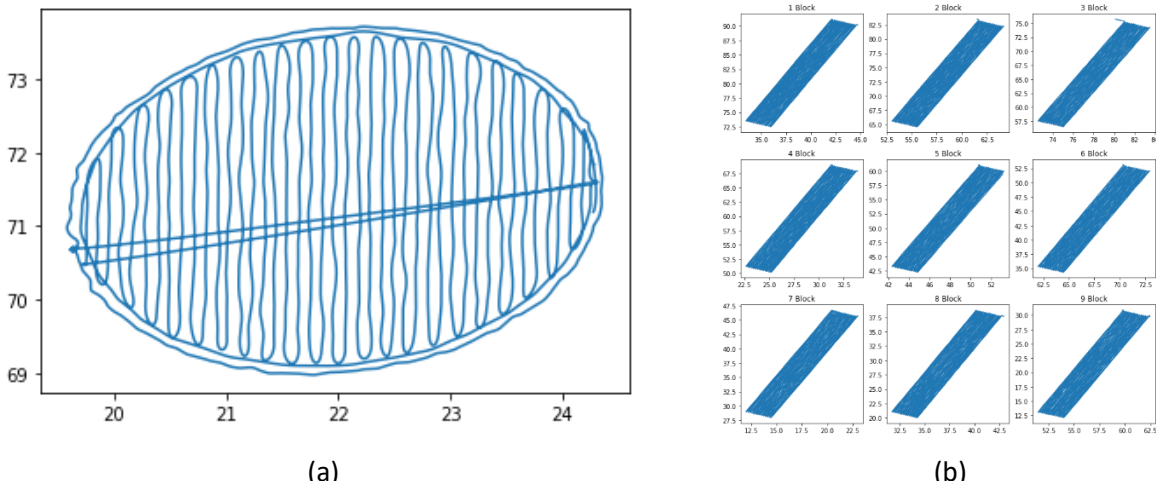


Figure 6.1.1 (a) Vertical Scan Path of training data (b) Slanted scan paths of testing data

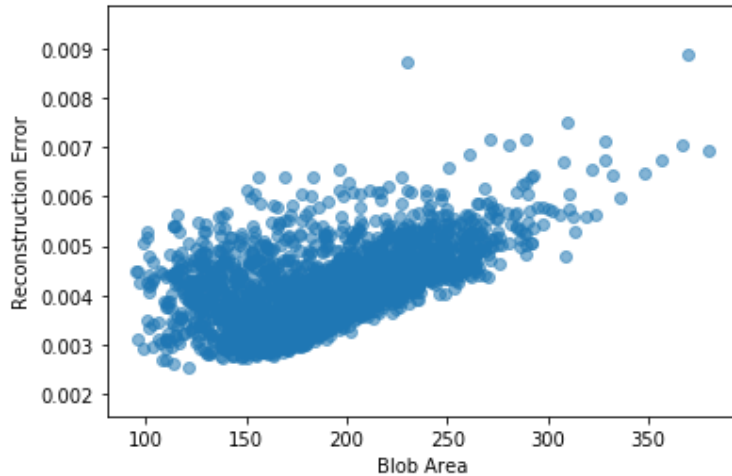


Figure 6.1.2 Scatter plot of RE against Blob Area of melt pool

As shown in Figure 6.1.2, the RE has slight positive correlation with the blob area (size of melt pool). In real settings, melt pools with abnormally large coverage have higher chance of being an anomaly (for example plume) but in general, due to the nature of one class classifier, this positive association can be attributed to the statistical behaviour of autoencoder that is, the model makes more error on average with more area to be reconstructed. For melt pool with smaller coverage but larger RE, the error is can be attributed to large quantity or area of spatter particles. For this reason, the usage of one class learning framework is just limited for spatter particles detection in this project.

As for the β -VAE, the topmost layer (L190) data was used as testing data while the training data consists of data from the layers below (L116 and L149). The training and testing of β -VAE was also made focus heights specific. In particularly, only block with focus heights of +4mm and -4mm were included as the melt pool images produced under 8mm focus height mostly contain of melt pool anomalies. With some trial-and-error, the level of disentanglement, β was set to be 5.0 for data of both focus heights. The distribution of the latent components for both focus heights are shown in Figure 6.1.3. As illustrated in Figure 6.1.4, specified ranges in the latent space were passed to the decoder for melt pool images generation to inspect the features captured by the β -VAE. The latent components represent the usual melt pool representations as before (Z1: Size, Z2: Roundness, Z3: Direction of Scan) although the disentanglement is visually less perfect.

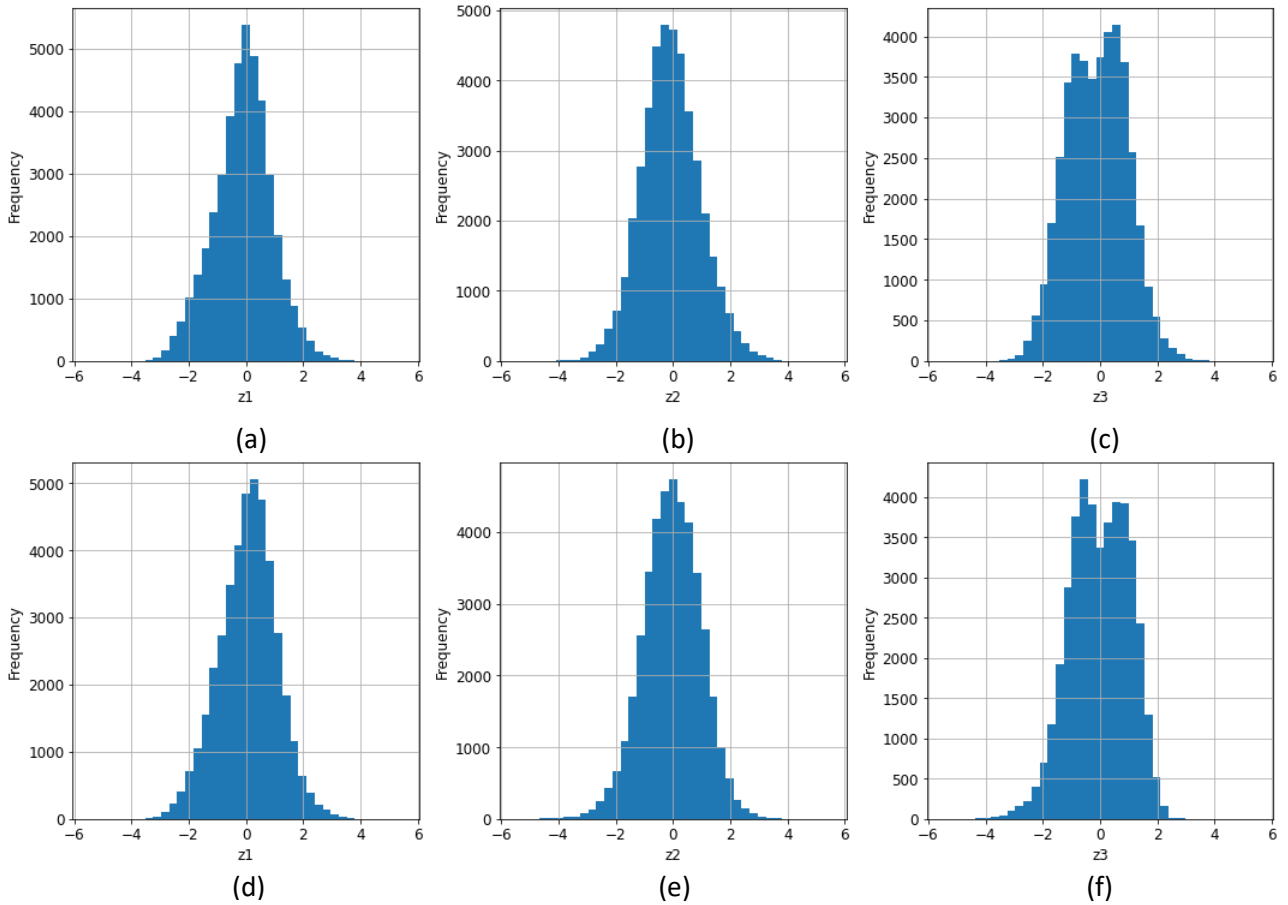


Figure 6.1.3(a)-(c) Latent Distributions for Build 2 Data with +4 mm Focus Height, (d)-(f) Latent Distributions for Build 2 Data with -4 mm Focus Height.

A case study was conducted particularly on the Block 4 of the new Build 2 Dataset. The microscopic image with -4mm focus height was used for the investigation between the occurrence of anomalies and defects formation. Appropriate transformations such as rotation and translations were applied to align the scan path coordinates with the microscopic image as illustrated in Figure 6.1.5(a). Figure 6.1.5(b) shows the original microscopic image as reference. Then, an interactive tool was built for the inspection of localised regions on the microscopic image. This tool allows its user to zoom into the microscopic image and select a few points within a specified radius of coverage for inspection. The radius of coverage was specified to be 50 units which, in most cases, captures at least 10 melt pool images from 3 individual scan tracks which are close to each other. The corresponding melt pool images in these selected regions will then be processed by the trained models including β -VAE, k-mean clustering and a supervised classifier for features extraction, anomaly metric computation, and anomalies classification respectively.

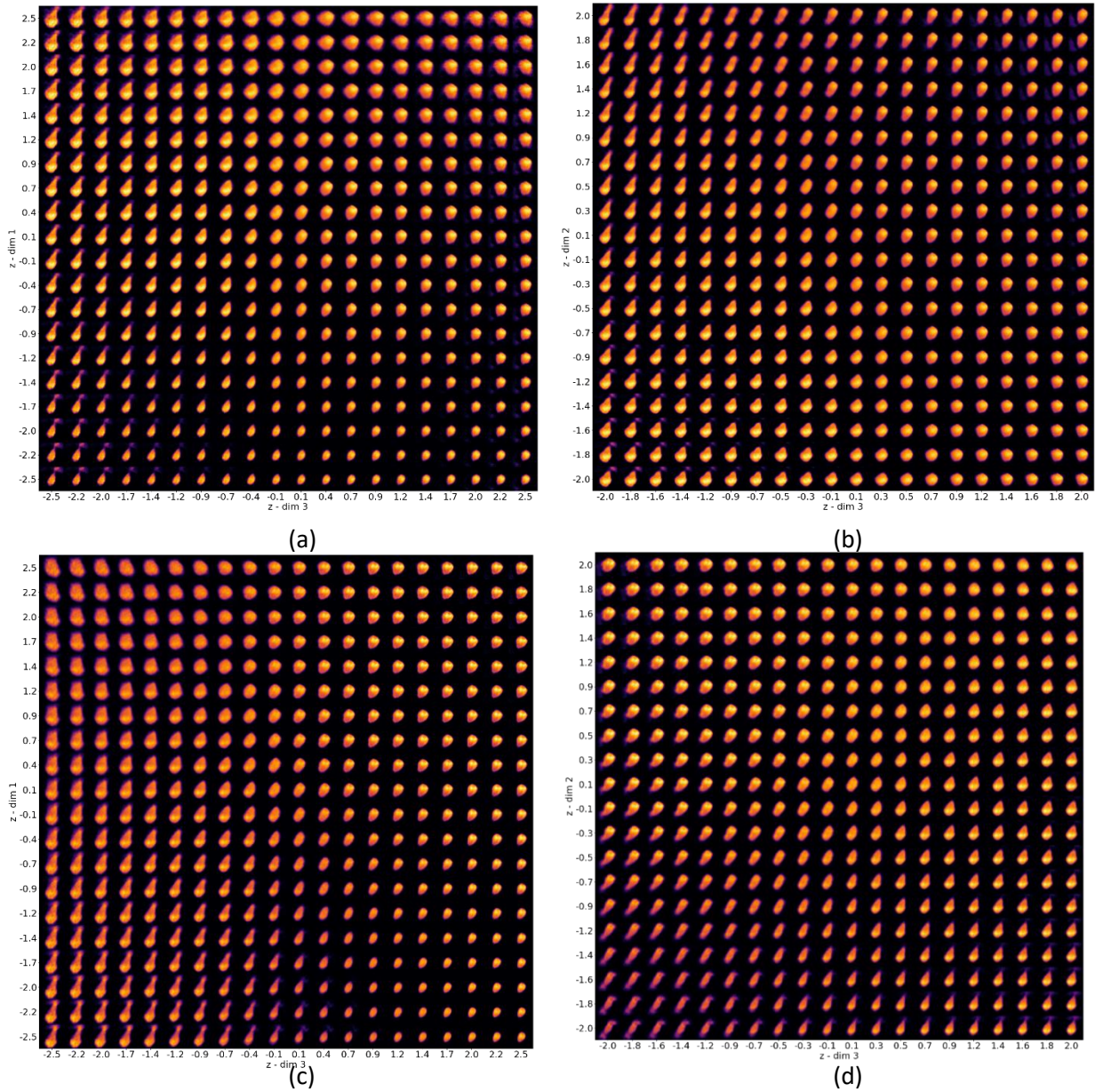


Figure 6.1.4 Grid plots of generated melt pool results for +4mm focus height dataset (a) Z_1 against Z_3 with $Z_2 = 0$, (b) Z_2 against Z_3 with $Z_1 = 0$; and for -4mm focus height dataset (c) Z_1 against Z_3 with $Z_2 = 0$, (d) Z_2 against Z_3 with $Z_1 = 0$.

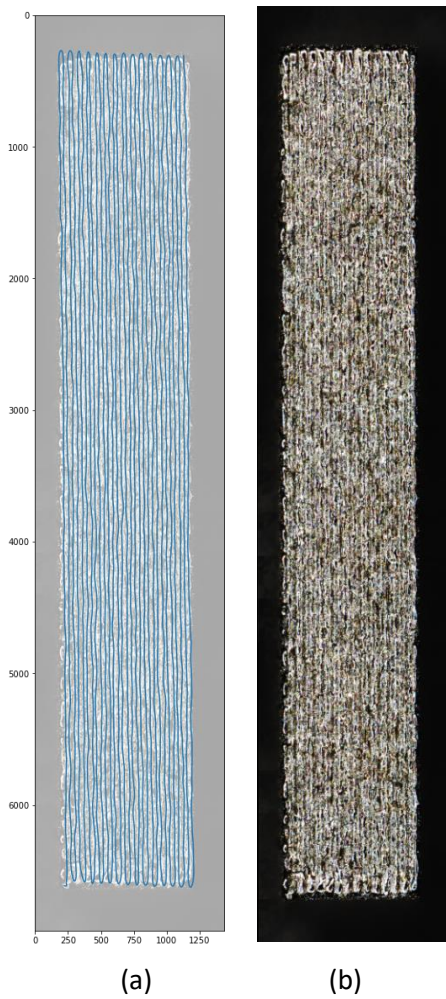


Figure 6.1.5 (a) Overlaid positional dataset and microscopic image and (b) Original microscopic image

6.2 Results

Figure 6.2.1 (a) shows the scan path with spatter particles detected. For spatter particles detection, the blob size of the melt pool was set to be smaller than the average melt pool size. Figure 6.2.1 (b) shows the melt pool frames with small blob size but high RE.

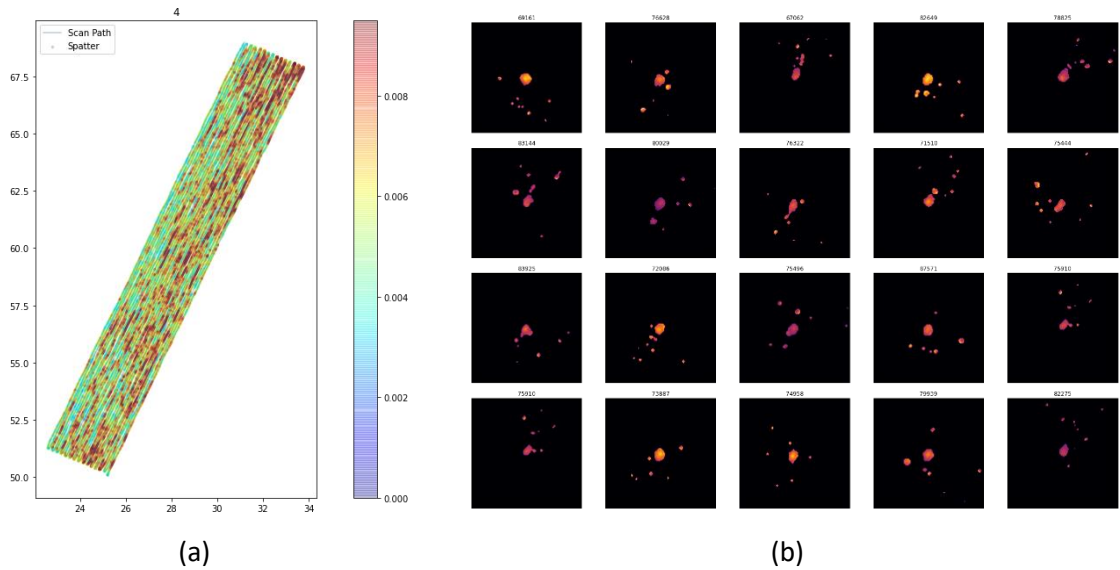


Figure 6.2.1 (a) Scan path with spatter particles detection, severity as reflected by the colour map of RE and (b) Spatter particles sampled from extreme cases of spatter.

As for the automated features extraction framework, a decision was taken to assign labels such as “unstable tail”, “large” and “plume” for melt pool with unstable tail (potentially having separating tail), large melt pools and plume instances. The classification results of the classifiers are summarised in the confusion matrices in Figure 6.2.2.

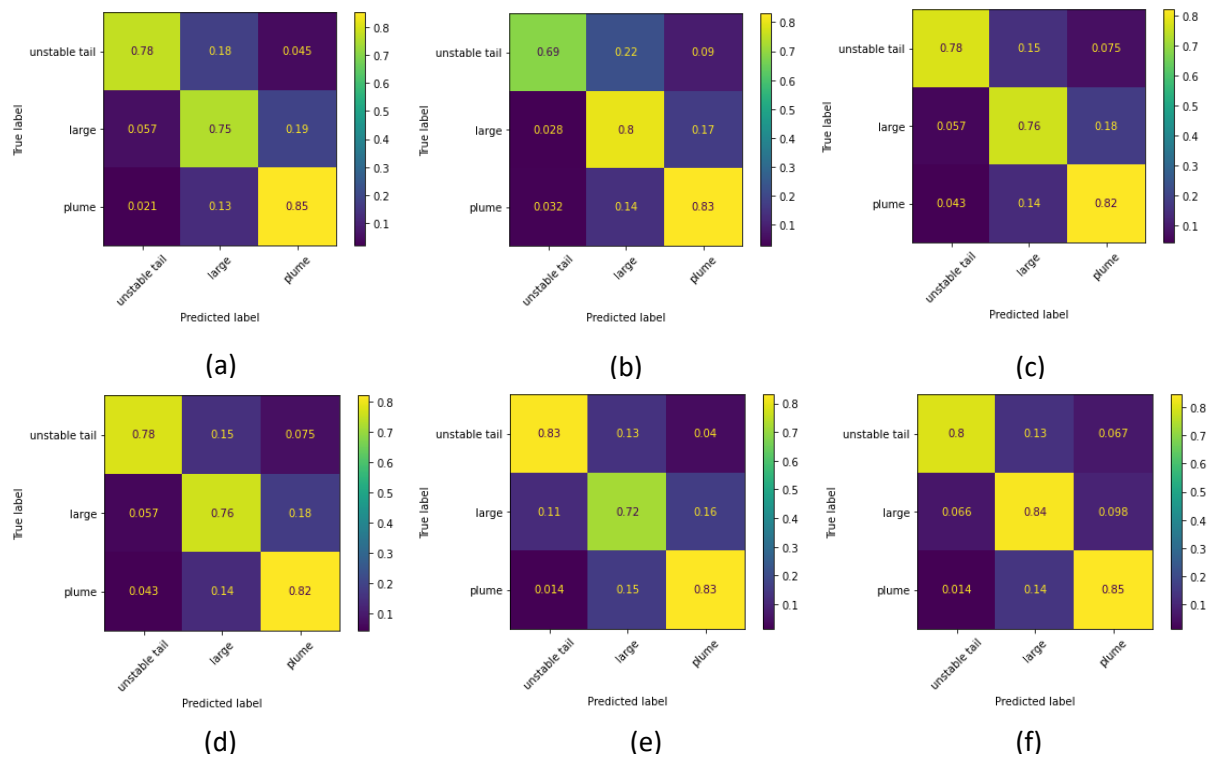


Figure 6.2.2 Confusion Matrices for Build 2 data classifications results. Focus height = +4mm (a)SVM, (b)KNN and (c)RF. Focus height = -4mm (d)SVM, (e) KNN and (f) RF.

For illustrations, the correct classifications of melt pools are presented as in Figure 6.2.3.

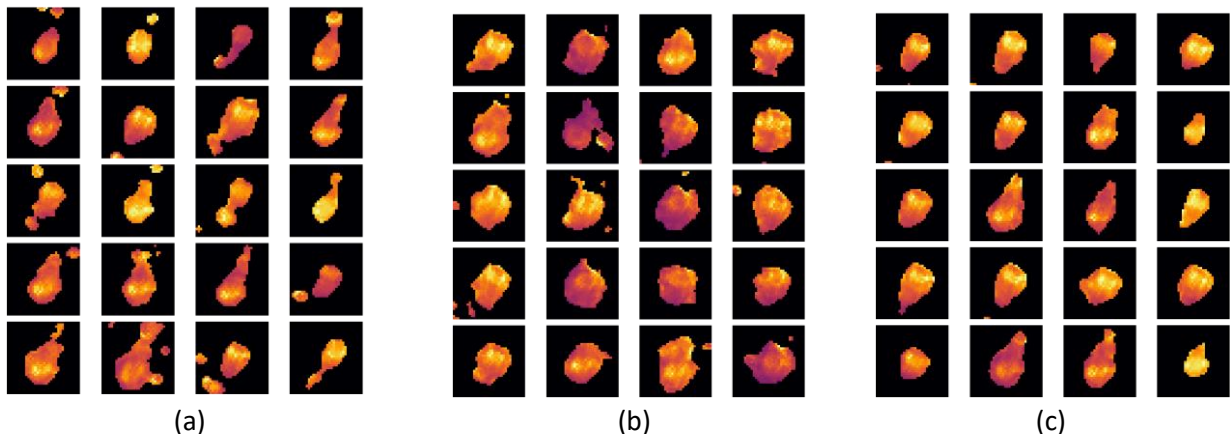


Figure 6.2.3 Build 2 Correct Classifications (a) Unstable Tail, (b) Plume and (c) Large melt pools.

For reference, the histogram of anomaly metric (distance of data points from respective cluster's centroid) for Block 4 is shown in Figure 6.2.4

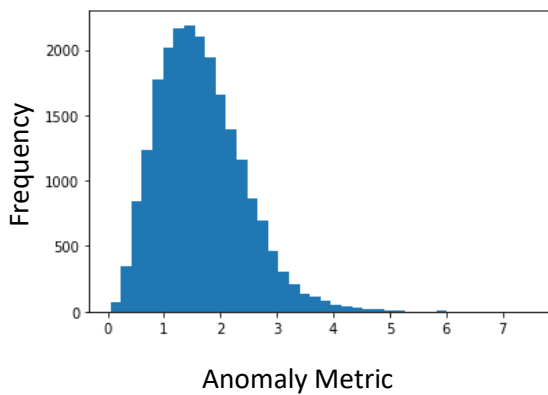
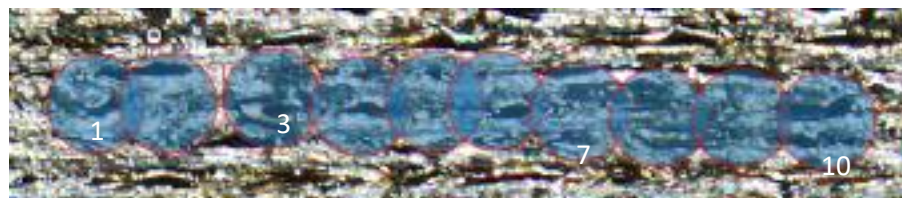


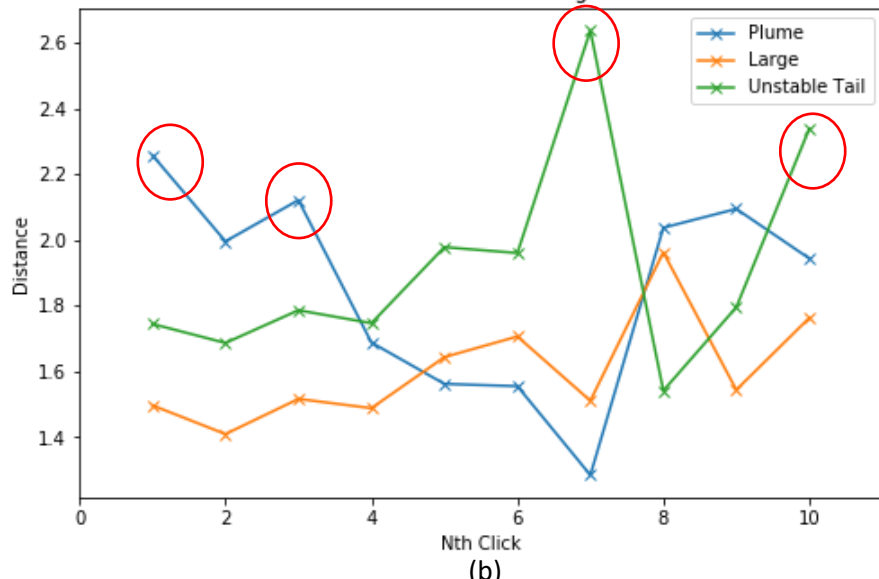
Figure 6.2.4 Distribution of anomaly metric (distance of data points from respective centroid).

A few caveats before some visualisations. Firstly, the dark patches on the microscopic images do not necessarily indicate holes or any other types of defects. They could be the shadowing effects from surrounding protrusions. However, since the scanning consists of straight scans, lateral dark regions which cross multiple tracks are most probably defects. Also, anomalous melt pools do not necessarily imply defects on the build – in fact following inspections aim to compare the occurrence of anomalies to the locations of defects on the build. Note that for melt pool frames sampled from the selection, the predicted classification results and anomaly metric are displayed on top of each image. For the computation of anomaly metric, the frames were aggregated based on classification results and then the mean of anomaly metric for each class was computed. For quick inspection, the computed average metric is not weighted for the number of class instances predicted. However, points are selected cautiously to avoid having too little frames for metric computations.

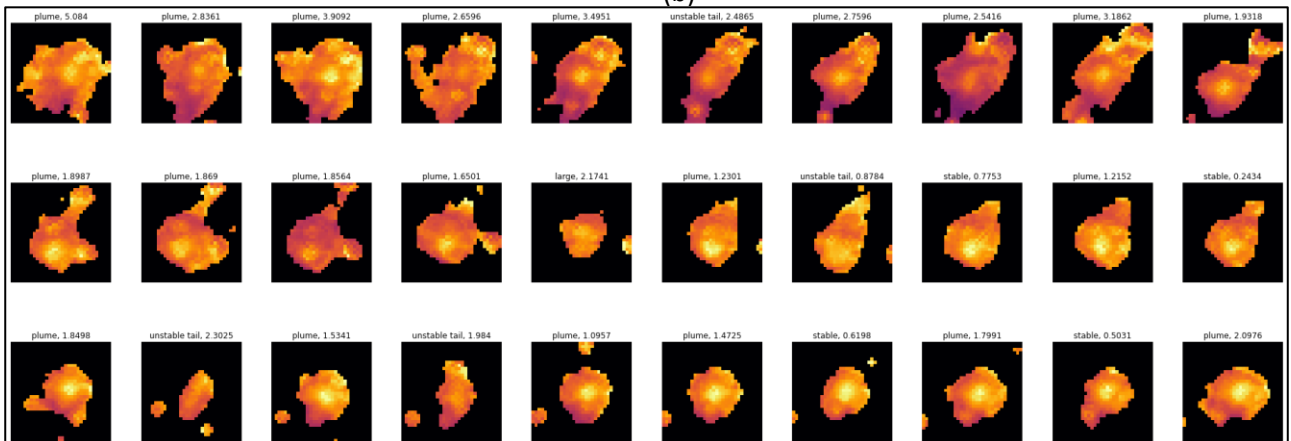


(a)

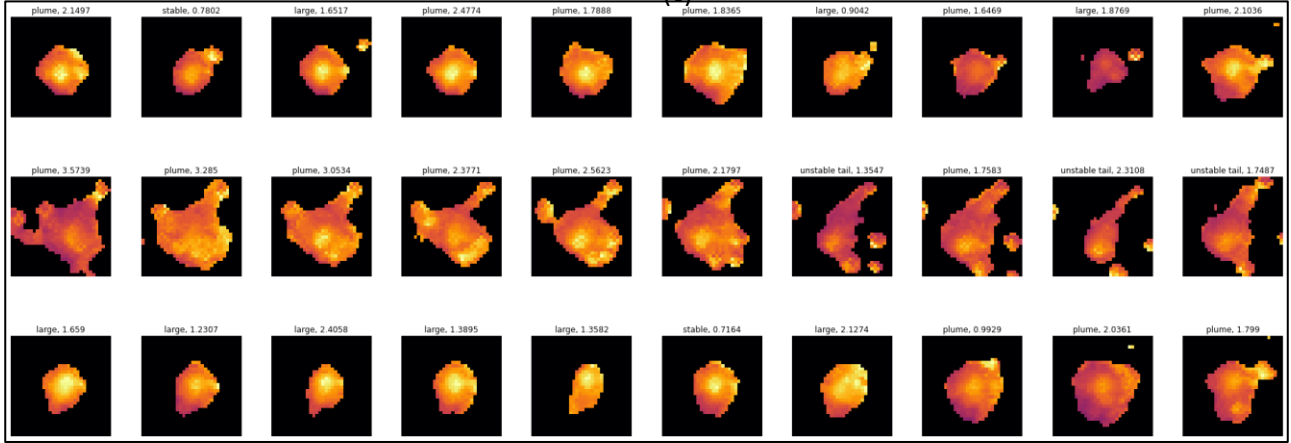
Variation of Anml Metric Along Scan Path



(b)



(c)



(d)

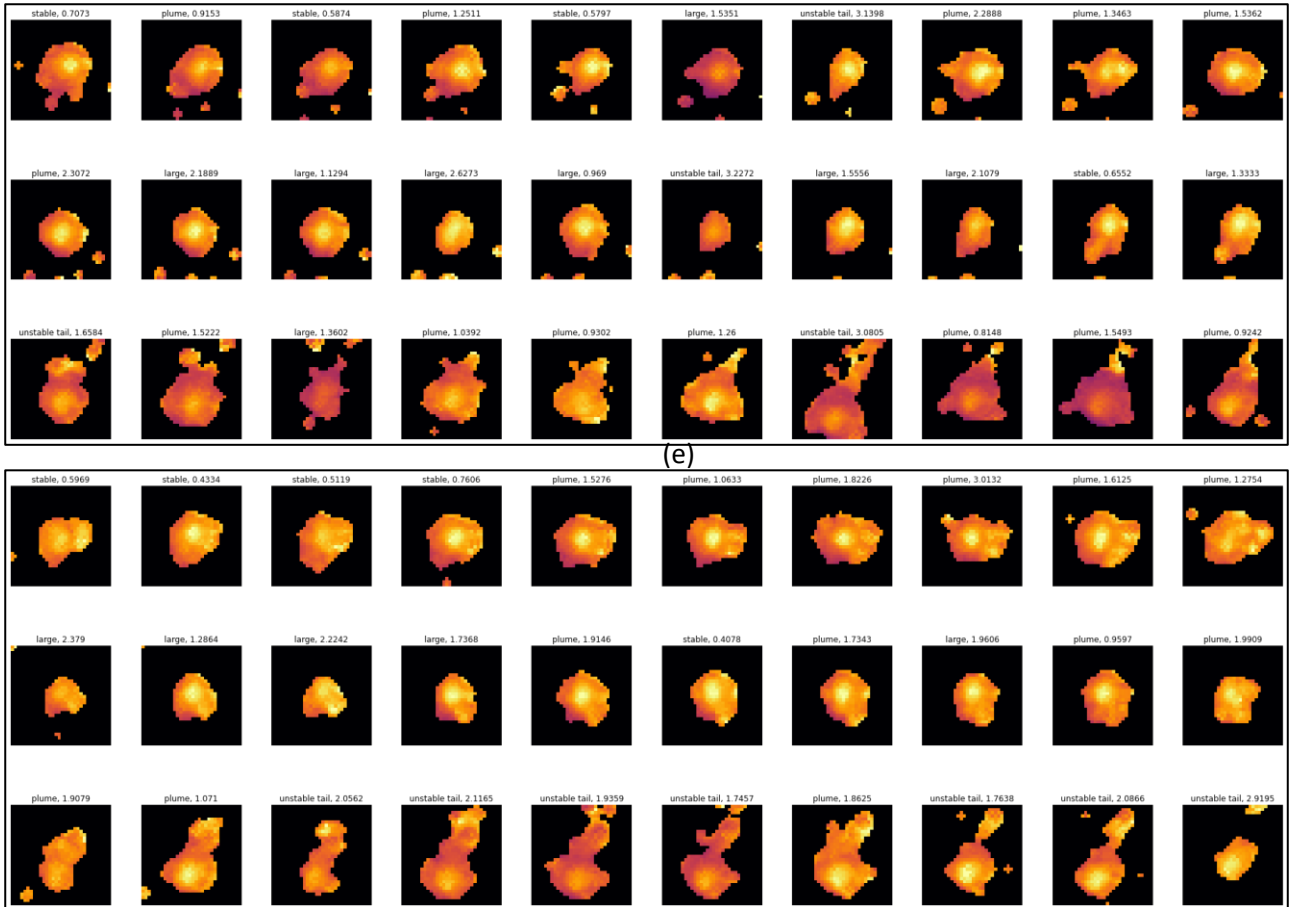
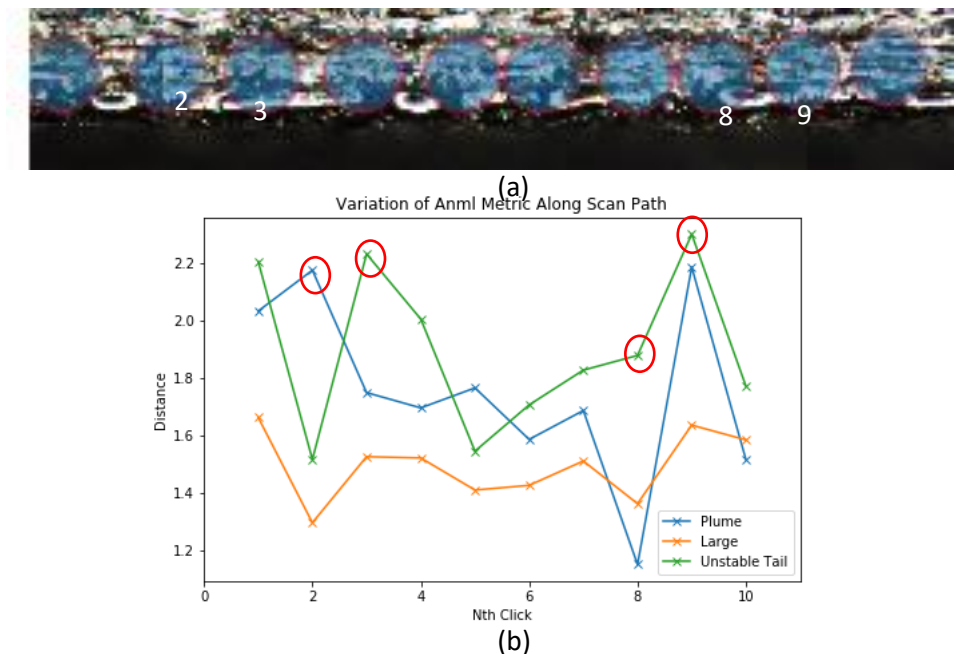
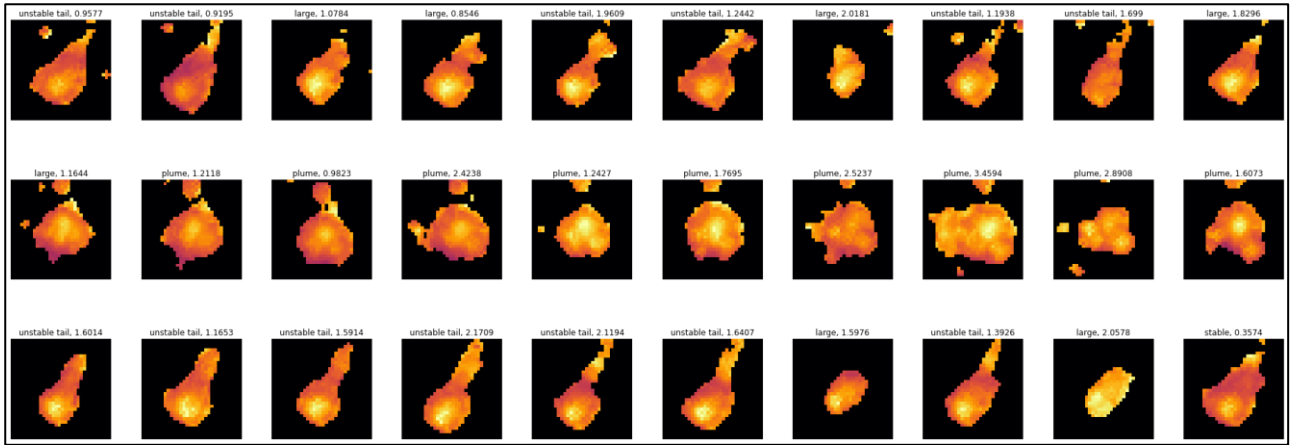
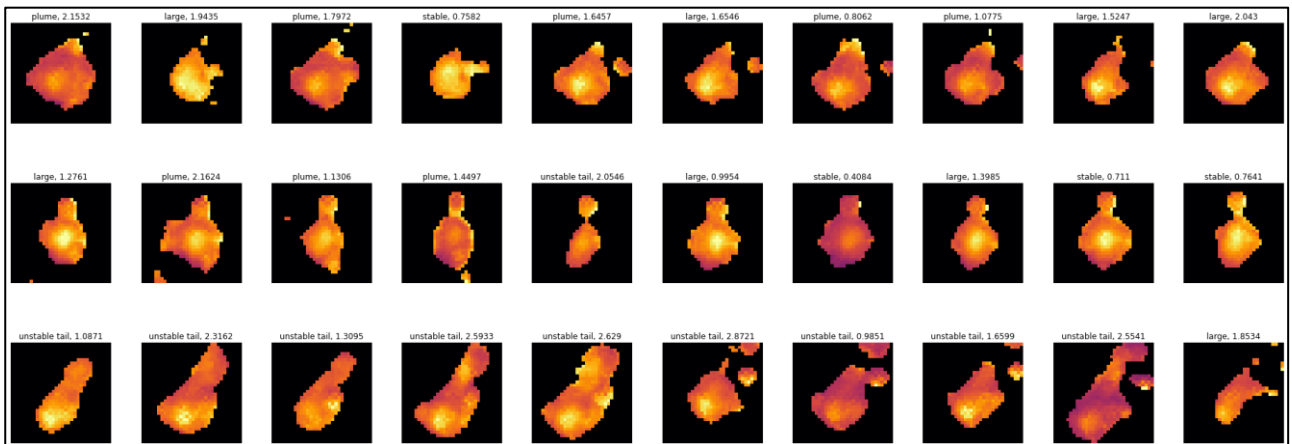


Figure 6.2.5 (a)Region of interest, (b) Variation of anomaly metrics, (c)-(f)Some melt pool images from 1st, 3rd, 7th and 10thselections respectively.

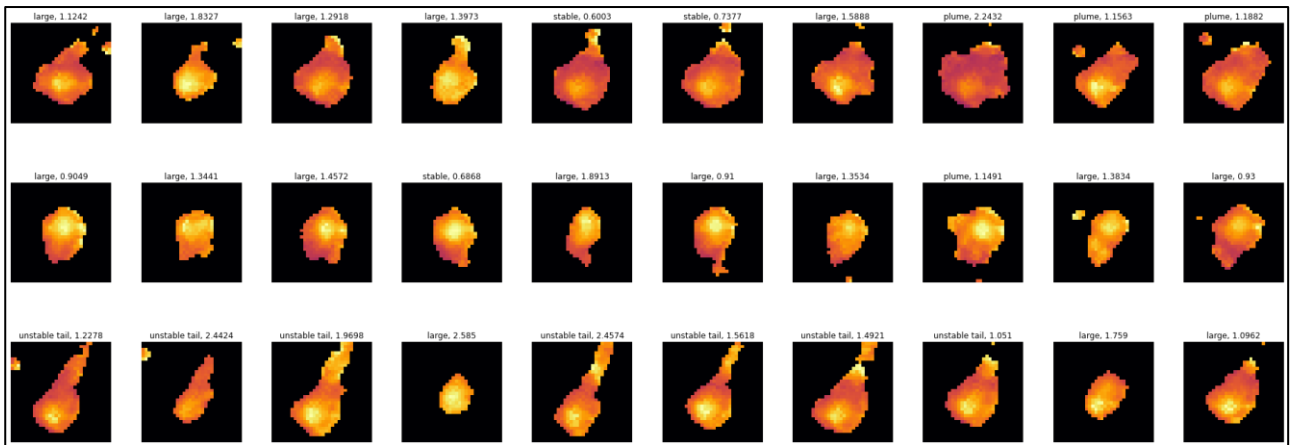




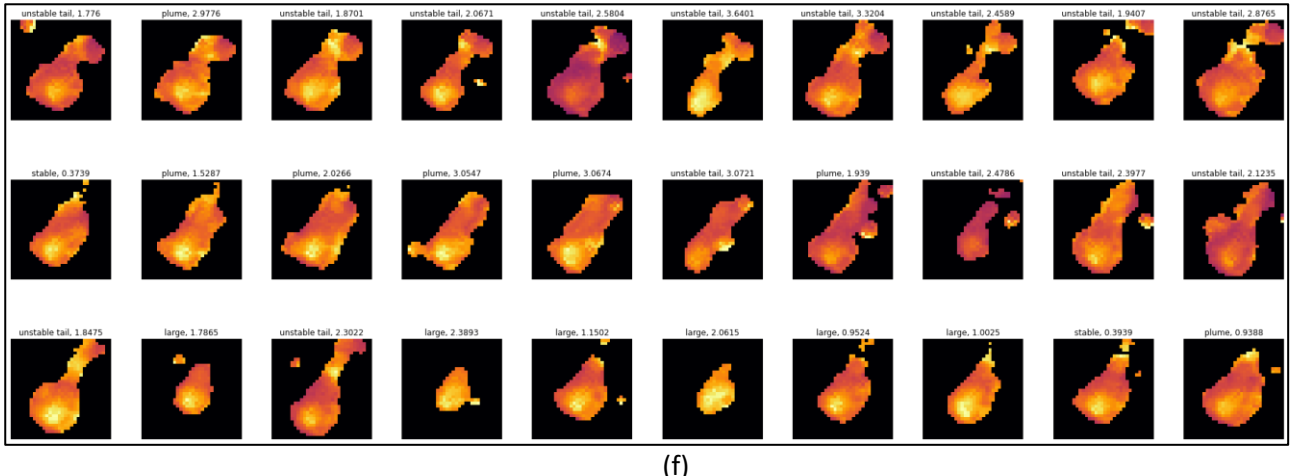
(c)



(d)



(e)



(f)

Figure 6.2.6 a)Region of interest, (b) Variation of anomaly metrics, (c)-(f)some melt pool images from 2nd, 3rd, 8thand 9th selections respectively.

To explore the correlation of the features extracted with depth data, the depth data was reflected and shifted so that the region's depths are represented by heights instead. Figure 6.2.7 (a) shows the microscopic image with its depth represented by the colour bar. The brighter the region is the higher the measure of depth. A few points were selected randomly for Pearson's correlation analysis as shown in Figure 6.2.7 (b). Note that the absolute value of Z3 was taken for correlations calculation as the sign of Z3 captures the direction and its magnitude represents the melt pool's tail length. The scatter plot of averaged latent components, Z1, Z2 and absolute Z3 is shown in Figure 6.2.8.

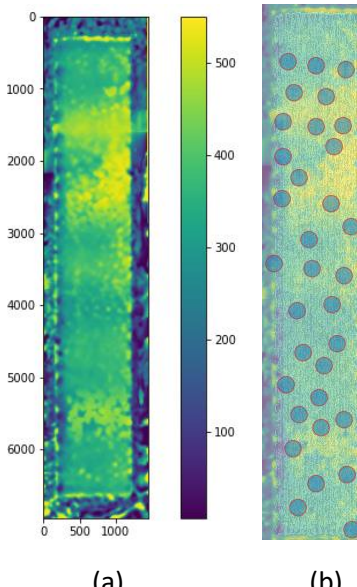


Figure 6.2.7 (a) The depth data, colour bar represents the magnitude of depth and (b) selected points for correlation analysis.

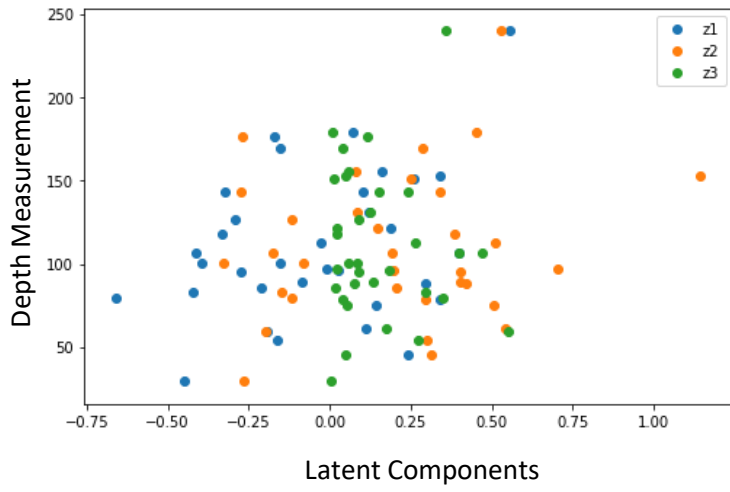


Figure 6.2.8 Scatter plot depth against Z1, Z2, and absolute Z3.

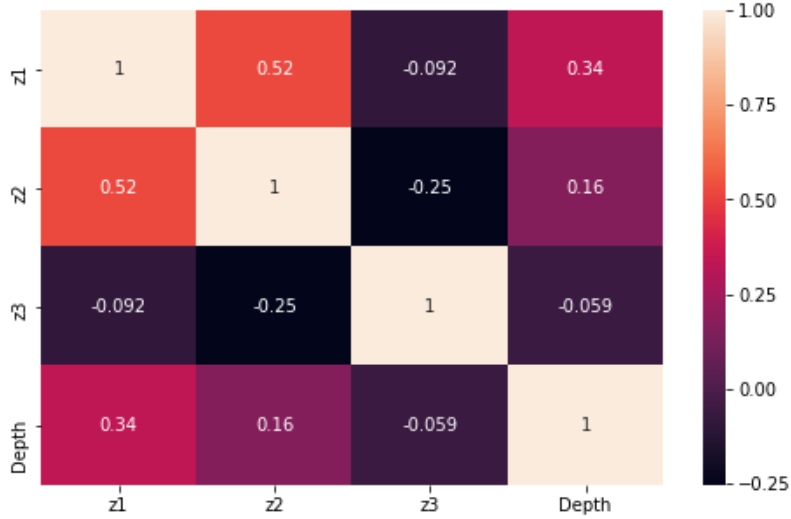


Figure 6.2.9 Correlations heatmap between Z1, Z2, Z3 and the depth data.

6.3 Discussions: Overlaid results

A few selections were shown. In Figure 6.2.5, the points of interests correspond to the 1st, 3rd, 7th and 10th selections. These points are selected for further inspections as they corresponds to spikes in the plume and unstable tail anomaly metrics. For example, large plume were found in the 1st and 3rd selections. The emission of plume accompanied by spatter ejections are probably the cause of dark patches (probably porosity) on the surface. Melt pools with highly unstable tail were also detected in the 7th and 10th selections. The occurrence of these unstable tails instances could be responsible for the dark patches on the surface. Similar observations were also observed in Figure 6.2.6, 2nd selection for spike in plume metric and 3rd, 8th and 9th selections for unstable tail.

Based on the correlation heat map in Figure 6.2.9, the first latent component, Z1 (captures the size of melt pool) seems to have slight positive association with depth. Also, Z1 and Z2(roundness of melt pools) have the highest positive correlations among all. For these selections, larger melt pools are generally rounder. As expected, Z2 is negatively correlated to absolute of Z3. This intuitively makes sense as melt pools with long tail tend to be not round.

7 Conclusion and Future Work Suggestion

7.1 Conclusion

Laser powder bed fusion is a relatively mature additive manufacturing technology. Despite that, the defects formation mechanisms during the printing process has not been fully understood. In the past, many have formulated theories to explain the formation of defects observed in the printed product. With coaxially resolved melt pool temperature profiles, this project aims to develop a set of metrics or machine learning frameworks to detect and classify various melt pool anomalies.

Starting from the exploratory data analysis, various anomalies such as plume, spattering and melt pool tail separation phenomena have been spotted. Metrics developed and region props features suggested that printing with 0mm and 4mm focus heights give the most stable melt pools. Following that, an anomaly detection framework centred around one class learning algorithm has been proposed. The training dataset was pre-sieved with K-Means Clustering to remove as many anomalous instances as possible. Next, a deep convolutional autoencoder was trained to ensure specialisation in reconstructing normal melt pool images. From various latent space visualisations, it was observed that some anomalies were still present in the training data. Hence, DBSCAN was used to further remove the remaining anomalies. The performance of autoencoder was compared against K-Means Clustering and DBSCAN-Autoencoder.

Motivated by the data compressing capability of an autoencoder, a second framework involving the probabilistic variant of autoencoder, the variational autoencoder was proposed. Specifically, a disentangled variational autoencoder was trained and used as a features-extractor for downstream melt pool anomalies classification task. By sampling from specified ranges of latent components, it was observed that the disentangled variational autoencoder captures the melt pool size, roundness and tail length. Using these encodings as learning features, classifiers such as k-Nearest Neighbours, Random Forest and Support Vector Machine shows great potential in classifying melt pool anomalies such as melt pool with unstable tail, large melt pools and plume. K-Means Clustering was employed to compute the distance of each data point from their respective cluster's centroid. This distance metric was used to quantify the degree of anomaly.

Both machine learning frameworks were then applied on new dataset to relate the occurrence of anomalies with the formation of defects. From the microscopic images, it was observed that tail separation and plume instances do correspond to dark patches or holes in the microscopic image of the scan. Although one cannot guarantee that those dark regions are defects, the supervised classifier at least produced a set of metrics which can be used to quantitatively describe and classify melt pool anomalies. Aside from that, the extracted latent components especially the one related to size also showed some positive correlation with the depth data provided.

7.2 Future work suggestions

Future work should include different melt pool geometries for the training of variational autoencoder. This is because the variational autoencoder learns the distribution of the underlying representations. Hence, give enough latent dimensions it should be able to cope with variations in melt pool geometries. Also, trained models can be deployed to a single-track scanning conducted with varying printing parameters. This will allow in detail investigation on how predicted melt pool geometries changes with the varying parameters and defects formed on the surface. Finally, the trained models can also be incorporated into a LPBF in-situ monitoring system to allow feedback control or to assess the final build quality.

8 References

1. P.A. Hooper, Melt pool temperature and cooling rates in laser powder bed fusion. *Additive Manufacturing*. 22 (2018) 548-59. <https://doi.org/10.1016/j.addma.2018.05.032>
2. R.J. Williams, A. Piglione, T. Rønnerberg, C. Jonnes, M.S Pham, C.M. Davies, P.A. Hooper, In-situ thermography for laser powder bed fusion: effects of layer temperature on porosity, microstructure and mechanical properties, *Additive Manufacturing* 30 (2019).
<https://doi.org/10.1016/j.addma.2019.100880>
3. S.A. Khairallah, A.T. Anderson, A. Rubenchik, W.E. King, Laser powder-bed fusion additive manufacturing: Physics of complex melt flow and formation mechanisms of pores, spatter, and denudation zones, *Acta Materialia* 108 (2016) 36–45.
<https://doi.org/10.1016/j.actamat.2016.02.014>
4. R. Rai, J.W. Elmer, T.A. Palmer, T.D. Roy, Heat transfer and fluid flow during keyhole mode laser welding of tantalum Ti-6Al-4V, 304L stainless steel and vanadium, *Journal of Physics D: Applied Physics*, 40 (2007) 5753-5766.
5. M.J. Matthews, G. Guss, S.A. Khairallah, A.M. Rubenchik, P.J. Depond, W.E. King, Denudation of metal powder layers in laser powder bed fusion process, *Acta Materialia*, 114 (2016) 33-42. <https://doi.org/10.1016/j.actamat.2016.05.017>
6. Y. Liu, Y. Yang, S. Mai, D. Wang, C. Song, Investigation into spatter behaviour during selective laser melting of AISI 316L stainless steel powder, *Materials & Design*, 87 (2015) 797-806. <https://doi.org/10.1016/j.matdes.2015.08.086>
7. M. Simonelli, C. Tuck, N.T. Aboulkhair, I. Maskery, R.D. Wildman, R. Hague, A study on the laser spatter and the oxidation reactions during selective laser melting of 316L stainless steel, Al-Si10-Mg, and Ti-6Al-4V, *Metall and Mat Trans A*, 46 (2015) 3842-3851.
<https://doi.org/10.1007/s11661-015-2882-8>
8. P. Bidare, I. Bitharas, R.M. Ward, M.M. Attallah, A.J. Moore, Fluid and particle dynamics in laser powder bed fusion. *Acta Materialia*. 142 (2018) 107-20.
<https://doi.org/10.1016/j.actamat.2017.09.051>
9. J.C. Fox, F. Lopez, B.M. Lane, H. Yeung, S. Grantham, On the requirements for model-based thermal control of melt pool geometry in Laser Powder Bed Fusion additive manufacturing, in: *Proceedings of the 2016 Material Science & Technology Conference* (2016) 133-140
10. J.P. Kruth, G. Levy, F. Klocke, T.H. Childs, Consolidation phenomena in laser and powder-bed based layered manufacturing. *CIRP annals*. 56 (2007) 730-59.
<https://doi.org/10.1016/j.cirp.2007.10.004>
11. J. Gockel, J. Beuth, K. Taminger, Integrated control of solidification microstructure and melt pool dimensions in electron beam wire feed additive manufacturing of Ti-6Al-4V. *Additive Manufacturing*. 119 (2014) 119-26. <https://doi.org/10.1016/j.addma.2014.09.004>
12. O. Simeone A very brief introduction to machine learning with applications to communication systems, 2018, <https://arxiv.org/abs/1808.02342>
13. A. Mujeeb, W. Dai, M. Erdt, A. Sourin. One class based feature learning approach for defect detection using deep autoencoders. *Advanced Engineering Informatics*. 42 (2019).
<https://doi.org/10.1016/j.aei.2019.100933>
14. F.T. Liu, K.M. Ting, Z.H. Zhou. Isolation forest, in: *2008 Eighth IEEE International Conference on Data Mining* (2008) 413-422. IEEE.

15. N. Abe, B. Zadrozny, J. Langford, Outlier detection by active learning, in: Proceedings of the 12th ACM SIGKDD international conference on Knowledge discovery and data mining (2006), 504-509
16. P.J. Rousseeuw, K.V. Driessen, A fast algorithm for the minimum covariance determinant estimator. *Technometrics.* 41 (1999) 212-23.
17. Y. Chen, X.S. Zhou, T.S. Huang, One-class SVM for learning in image retrieval. InProceedings 2001 International Conference on Image Processing 1 (2001), 34-37. doi: 10.1109/ICIP.2001.958946.
18. E.M. Knox, R.T. Ng, Algorithms for mining distance based outliers in large datasets. InProceedings of the international conference on very large data bases (1998) 392-403
19. J.A. Kanko, A.P. Sibley, J.M. Fraser, In situ morphology-based defect detection of selective laser melting through inline coherent imaging, *Journal of Materials Processing Technology,* 231 (2016) 488-500. <https://doi.org/10.1016/j.jmatprotec.2015.12.024>
20. B. Lane, S. Moylan, E.P. Whitenton, L. Ma. Thermographic measurements of the commercial laser powder bed fusion process at NIST, *Rapid Prototyping Journal,* 22 (2015) 778-787. <https://doi.org/10.1108/RPJ-11-2015-0161>
21. S.A. Shevchik, C. Kenel, C. Leinenbach, K. Wasmer, Acoustic emission for in situ quality monitoring in additive manufacturing using spectral convolutional neural networks, *Additive Manufacturing,* 21 (2018) 598-604.
22. H. Rieder, A. Dillhöfer, M. Spies, J. Bamberg, T. Hess, Ultrasonic online monitoring of additive manufacturing processes based on selective laser melting. InAIP Conference Proceedings 1650 (2015) 184-191. <https://doi.org/10.1063/1.4914609>
23. G. Repossini, V. Laguzza, M. Grasso, B.M. Colosimo. On the use of spatter signature for in-situ monitoring of Laser Powder Bed Fusion, *Additive Manufacturing.* 16 (2017) 35-48. <https://doi.org/10.1016/j.addma.2017.05.004>
24. Y. Zhang, G.S. Hong, D. Ye, K. Zhu, J.Y. Fuh. Extraction and evaluation of melt pool, plume and spatter information for powder-bed fusion AM process monitoring. *Materials & Design.* 156 (2018) 458-69. <https://doi.org/10.1016/j.matdes.2018.07.002>
25. M. Grasso, V. Laguzza, Q. Semeraro, B.M. Colosimo, In-process monitoring of selective laser melting: spatial detection of defects via image data analysis. *Journal of Manufacturing Science and Engineering.* 5 (2017) 139. <https://doi.org/10.1115/1.4034715>
26. S.S. Khan, M.G. Madden, One-class classification: taxonomy of study and review of techniques, *The Knowledge Engineering Review,* 3 (2014) 345-74. <https://doi.org/10.1017/S02698891300043X>
27. P. Bholowalia, A. Kumar, EBK-means: A clustering technique based on elbow method and k-means in WSN, *International Journal of Computer Applications,* 9 (2014).
28. T. Fawcett, An introduction to ROC analysis, *Pattern recognition letters,* 27 (2006) 861-74. <https://doi.org/10.1016/j.patrec.2005.10.010>
29. I. Higgins, L. Matthey, X. Glorot, A. Pal, B. Uria, C. Blundell, S. Mohamed, A. Lerchner, Early visual concept learning with unsupervised deep learning (2016). <https://arxiv.org/abs/1606.05579>